

Two Peculiar Fast Transients in a Strongly Lensed Host Galaxy

S. A. RODNEY^{1,2,3}, I. BALESTRA⁴, M. BRADAC⁵, G. BRAMMER⁶, T. BROADHURST^{7,8}, G. B. CAMINHA⁹, G. CHIRIVI¹⁰, J. M. DIEGO¹¹, A. V. FILIPPENKO¹², R. J. FOLEY^{13,14,15}, O. GRAUR^{16,17,18}, C. GRILLO¹⁹, S. HEMMATI²⁰, J. HJORTH¹⁹, A. HOAG⁵, M. JAUCZAC^{21,22,23}, S. W. JHA²⁴, R. KAWAMATA²⁵, P. L. KELLY¹², C. MCCULLY^{26,27}, B. MOBASHER²⁸, A. MOLINO^{29,30}, M. OGURI^{31,32,33}, A. G. RIESS^{1,6}, P. ROSATI⁹, K. B. SCHMIDT^{27,34}, J. SELSING¹⁹, K. SHARON³⁵, L.-G. STROLGER⁶, S.-H. SUYU^{10,36,37}, T. TREU^{38,39}, B. J. WEINER⁴⁰, L. L. R. WILLIAMS⁴¹, AND A. ZITRIN^{20,42,2}

Draft version May 10, 2017

ABSTRACT

Two unusual transient events were observed by the Hubble Space Telescope in 2014, appearing in a galaxy at $z = 1.0054 \pm 0.0002$ that is gravitationally lensed by the galaxy cluster MACS0416. These transients—collectively nicknamed “Spock”—were faster and fainter than any supernova, but significantly more luminous than a classical nova: they reached peak luminosities of $\sim 10^{41}$ erg s⁻¹ ($M_{AB} < -14$) in $\lesssim 5$ rest-frame days, then faded below detectability in roughly the same time span. Lens models of the foreground cluster suggest that it is entirely plausible that the two events are *spatially* coincident at the source plane, but very unlikely that they were also *temporally* coincident. We find that *Spock* can be explained as a luminous blue variable, a recurrent nova, or a pair of stellar microlensing events. High-cadence monitoring of the field could help to distinguish between these hypotheses by detecting new transient episodes at or near the HFF14Spo locations. Improvements to the lens models are also needed to clarify the position of the critical curves.

¹ Department of Physics and Astronomy, The Johns Hopkins University, 3400 N. Charles St., Baltimore, MD 21218, USA

² Hubble Fellow

³ Department of Physics and Astronomy, University of South Carolina, 712 Main St., Columbia, SC 29208, USA

⁴ University Observatory Munich, Scheinerstrasse 1, D-81679 Munich, Germany

⁵ University of California Davis, 1 Shields Avenue, Davis, CA 95616

⁶ Space Telescope Science Institute, 3700 San Martin Dr., Baltimore, MD 21218, USA

⁷ Fisika Teorikoa, Zientzia eta Teknologia Fakultatea, Euskal Herriko Unibertsitatea UPV/EHU

⁸ IKERBASQUE, Basque Foundation for Science, Alameda Urquijo, 36-5 48008 Bilbao, Spain

⁹ Dipartimento di Fisica e Scienze della Terra, Università degli Studi di Ferrara, via Saragat 1, I-44122, Ferrara, Italy

¹⁰ Max-Planck-Institut für Astrophysik, Karl-Schwarzschild-Str. 1, 85748 Garching, Germany

¹¹ IFCA, Instituto de Física de Cantabria (UC-CSIC), Av. de Los Castros s/n, 39005 Santander, Spain

¹² Department of Astronomy, University of California, Berkeley, CA 94720-3411, USA

¹³ Department of Physics, University of Illinois at Urbana-Champaign, 1110 W. Green Street, Urbana, IL 61801, USA

¹⁴ Astronomy Department, University of Illinois at Urbana-Champaign, 1002 W. Green Street, Urbana, IL 61801, USA

¹⁵ University of California Santa Cruz, 1156 High St, Santa Cruz, CA 95064

¹⁶ Center for Cosmology and Particle Physics, New York University, New York, NY 10003, USA

¹⁷ Department of Astrophysics, American Museum of Natural History, Central Park West and 79th Street, New York, NY 10024, USA

¹⁸ Harvard/Smithsonian Center for Astrophysics, Cambridge, MA 02138, USA

¹⁹ Dark Cosmology Centre, Niels Bohr Institute, University of Copenhagen, Juliane Maries Vej 30, DK-2100 Copenhagen, Denmark

²⁰ Cahill Center for Astronomy and Astrophysics, California Institute of Technology, MC 249-17, Pasadena, CA 91125, USA

²¹ Centre for Extragalactic Astronomy, Department of Physics, Durham University, Durham DH1 3LE, U.K.

²² Institute for Computational Cosmology, Durham University, South Road, Durham DH1 3LE, U.K.

²³ Astrophysics and Cosmology Research Unit, School of

Mathematical Sciences, University of KwaZulu-Natal, Durban 4041, South Africa

²⁴ Department of Physics and Astronomy, Rutgers, The State University of New Jersey, Piscataway, NJ 08854, USA

²⁵ Department of Astronomy, Graduate School of Science, The University of Tokyo, 7-3-1 Hongo, Bunkyo-ku, Tokyo 113-0033, Japan

²⁶ Las Cumbres Observatory Global Telescope Network, 6740 Cortona Dr., Suite 102, Goleta, California 93117, USA

²⁷ Department of Physics, University of California, Santa Barbara, CA 93106-9530, USA

²⁸ Department of Physics and Astronomy, University of California, Riverside, CA 92521, USA

²⁹ Instituto de Astronomía, Geofísica e Ciências Atmosféricas, Universidade de São Paulo, Cidade Universitária, 05508-090, São Paulo, Brazil

³⁰ Instituto de Astrofísica de Andalucía (CSIC), E-18080 Granada, Spain

³¹ Research Center for the Early Universe, University of Tokyo, 7-3-1 Hongo, Bunkyo-ku, Tokyo 113-0033, Japan

³² Department of Physics, University of Tokyo, 7-3-1 Hongo, Bunkyo-ku, Tokyo 113-0033, Japan

³³ Kavli Institute for the Physics and Mathematics of the Universe (Kavli IPMU, WPI), University of Tokyo, 5-1-5 Kashiwanoha, Kashiwa, Chiba 277-8583, Japan

³⁴ Leibniz-Institut für Astrophysik Potsdam (AIP), An der Sternwarte 16, 14482 Potsdam, Germany

³⁵ Department of Astronomy, University of Michigan, 1085 S. University Avenue, Ann Arbor, MI 48109, USA

³⁶ Institute of Astronomy and Astrophysics, Academia Sinica, P.O. Box 23-141, Taipei 10617, Taiwan

³⁷ Physik-Department, Technische Universität München, James-Franck-Straße 1, 85748 Garching, Germany

³⁸ Department of Physics and Astronomy, University of California, Los Angeles, CA 90095

³⁹ Packard Fellow

⁴⁰ Department of Astronomy, University of Arizona, Tucson, AZ 85721, USA

⁴¹ School of Physics and Astronomy, University of Minnesota, 116 Church Street SE, Minneapolis, MN 55455, USA

⁴² Ben-Gurion University of the Negev P.O.B. 653 Beer-Sheva 8410501, Israel

1. INTRODUCTION

The Spock transient events—separately designated HFF14Spo-NW and HFF14Spo-SE—appeared in Hubble Space Telescope (*HST*) imaging collected in January and August of 2014, respectively (Figure 1). These observations were centered on the galaxy cluster MACS J0416.1-2403 (hereafter, MACS0416) and were collected as part of the Hubble Frontier Fields (HFF) survey (HST-PID:13496, PI:Lotz), a multi-cycle program for deep imaging of 6 massive galaxy clusters and associated “blank sky” fields observed in parallel (Methods 4.1).

Combining the *HST* imaging and lens models of the MACS0416 gravitational lens leads to three key observables for the HFF14Spo events: (1) they are both more luminous than a classical nova, but less luminous than almost all supernovae (SNe), reaching a peak luminosity of roughly 10^{41} erg s $^{-1}$ ($M_V = 14$); (2) both transients exhibited fast light curves, with rise and decline timescales of \sim 2–5 days in the rest frame; and (3) it is likely that both events arose from the same physical location but were not coincident in time—they were probably separated by 3–5 months in the rest frame. These peculiar transients thus present an intriguing puzzle: they are broadly consistent with the expected behavior of stellar explosions (they each exhibit a single isolated rise and decline in brightness), but they can not be trivially classified into any of the common categories of explosive or eruptive astrophysical transients.

The HFF survey was not designed with the discovery of peculiar extragalactic transients as a core objective, but it has unintentionally opened an effective window of discovery for such events. Very faint sources at relatively high redshift ($z \gtrsim 1$) in these fields are made detectable by the substantial gravitational lensing magnification from the foreground galaxy clusters. Very rapidly evolving sources are also more likely to be found, due to the necessity of a rapid cadence for repeat imaging in the HFF program. These unusual characteristics for an *HST* survey enabled a precise measurement of the lensing magnification for SN Tomas, a high-redshift thermonuclear (Type Ia) SN (Rodney *et al.* 2015). The HFF imaging program also contributed to the detection and characterization of SN Refsdal, a high-redshift core-collapse SN and the first strongly-lensed SN observed with multiple resolved images (Kelly *et al.* 2015). The long-term monitoring campaign of SN Refsdal then led to the discovery of the peculiar lensed transient *Icarus*, which is posited to be a stellar caustic crossing event (Kelly *et al.* 2017). Even among this collection of rare transients, the HFF14Spo events appear to be *sui generis*. No single astrophysical model is clearly sufficient to explain all of the available observational data, and the best available models require either an extreme stellar source or a very unusual gravitational lensing configuration.

2. RESULTS

Photometry collected from the *HST* images (Methods 4.2), reveals that the two HFF14Spo both exhibited very rapid light curves, as shown in Figure 2. Both events reached a peak luminosity of \sim 0.08 μ Jy, with the entire observable rise and fall occurring in < 20 days. The host galaxy for both HFF14Spo events is at a redshift of $z = 1.0054 \pm 0.0002$ (Methods 4.3). After dividing the

observed timescales by $(1+z)$ to correct for cosmic time dilation, we see that both events lasted < 10 days in the rest frame.

To interpret the observed light curves and the timing of these two events, we use seven independently constructed cluster mass models to determine the impact of gravitational lensing from the MACS0416 cluster (Methods 4.4). The lensing configuration that has been consistently adopted for this cluster assumes that the arc in which the HFF14Spo events appeared consists of two mirror images of the host galaxy, labeled 11.1 and 11.2 in Figure 1 (Zitrin *et al.* 2013; Jauzac *et al.* 2014; Johnson *et al.* 2014; Richard *et al.* 2014; Diego *et al.* 2015; Grillo *et al.* 2015; Hoag *et al.* 2016; Sebesta *et al.* 2016; Caminha *et al.* 2017). This implies that a single critical curve passes roughly mid-way between the two observed HFF14Spo locations.

In Table 1 we report model-predicted time delays relative to the HFF14Spo-NW event, which appeared in January 2014 in host image 11.2. We also report absolute magnification values between about $\mu = 10$ and $\mu = 300$ for both events. This wide range is due primarily to the close proximity of the HFF14Spo events to the lensing critical curve (the region of theoretically infinite magnification) for sources at $z = 1$. The location of the critical curve relative to each HFF14Spo event varies significantly among the models, and is sensitive to many parameters that are poorly constrained. We have explored model variations (described in Methods 4.5) that adjust the cluster redshift and the masses of cluster member galaxies, and that account for the impact of lensing perturbations from galaxies along the line of sight. Most variations that move a critical curve closer to the position of HFF14Spo-NW would drive the magnification of that event much higher (toward $\mu_1 \sim 300$). This generally also has the effect of moving the critical curve farther from HFF14Spo-SE, which would necessarily drive its magnification downward (toward $\mu_2 \sim 10$). Our model variations also show that it is possible to make reasonable adjustments to the lens model parameters in order to ensure that a critical curve intersects both of the HFF14Spo locations. Such lensing configurations can qualitatively reproduce the observed morphology of the HFF14Spo host galaxy, but they are disfavored by a purely quantitative assessment of the positional strong-lensing constraints.

Figure 2 shows that the observed peak brightnesses for the two events agree to within $\sim 30\%$, which means that if these represent a single source then a factor of 10 difference in magnification would have to be compensated by a correspondingly steep slope in the intrinsic SED of the source from rest-frame UV to optical wavelengths.

2.1. Ruling Out Common Astrophysical Transients

There are several categories of astrophysical transients that cannot accommodate the light curve characteristics of the HFF14Spo transients. We may first dismiss any of the category of *periodic* sources (e.g. Cepheids, RR Lyrae, or Mira variables) that exhibit regular changes in flux due to pulsations of the stellar photosphere. These variable stars do not exhibit sharp, isolated transient episodes that could match the HFF14Spo light curve shapes. Stellar flares provide another very common source for optical transient events, but the total energy

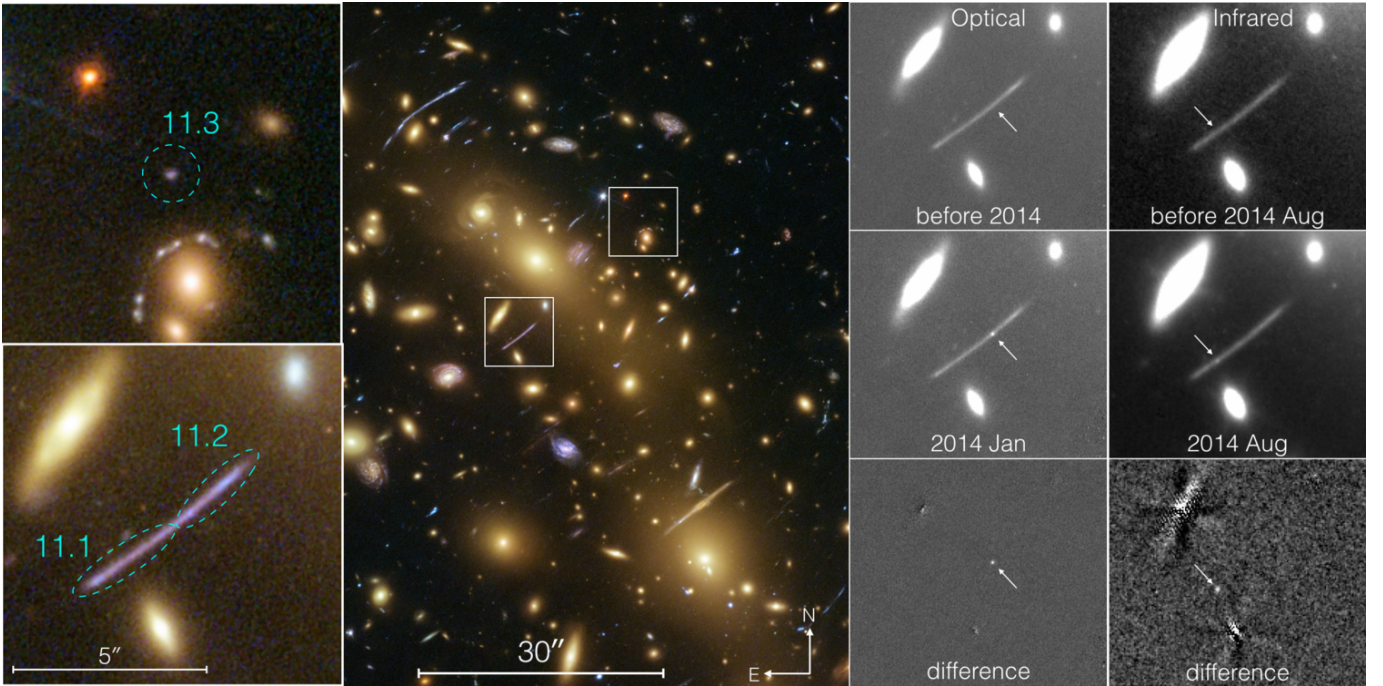


FIG. 1.— The detection of HFF14Spo-NW and HFF14Spo-SE in HST imaging from the Hubble Frontier Fields. The central panel shows the full field of the MACSJ0416 cluster, in a combined image using optical and infrared bands from HST. Two boxes within the main panel demarcate the regions where the HFF14Spo host galaxy images appear. These regions are shown as two inset panels on the left, highlighting the three images of the host galaxy (labeled 11.1, 11.2, and 11.3), which are caused by the gravitational lensing of the cluster. Two columns on the right side show the discovery of the two transient events in optical and infrared light, respectively. In these final two columns the top row is a template image, the center row shows the epoch when each transient appeared, and the bottom row is the difference image.

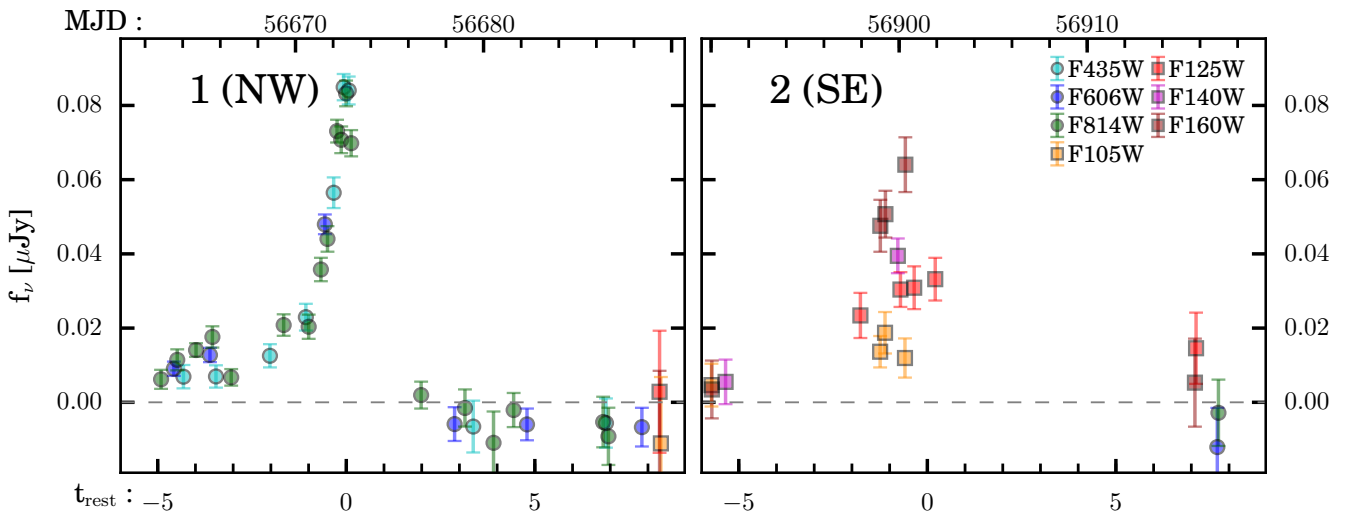


FIG. 2.— Light curves for the two transient events, HFF14Spo-NW on the left and HFF14Spo-SE on the right. Measured fluxes in micro-Janskys are plotted against rest-frame time at $z = 1.0054$, relative to the time of the peak observed flux for each event. The corresponding Modified Julian Date (MJD) in the observer frame is marked on the top axis for each panel. As indicated in the legend, optical observations using the *HST* ACS-WFC detector are plotted as circles, while infrared measurements from the WFC3-IR detector are plotted as squares.

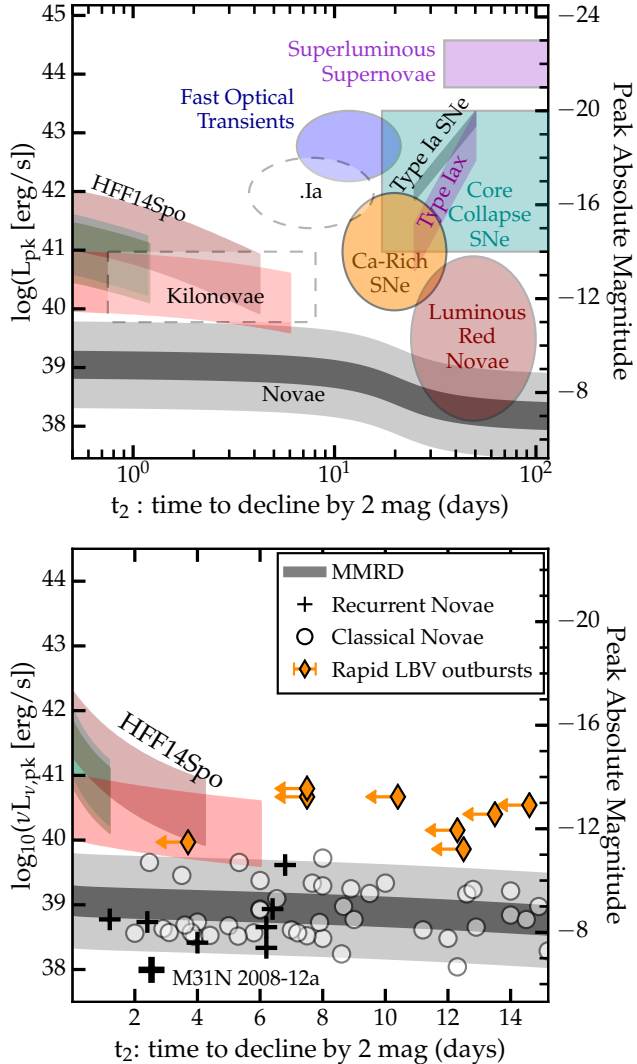


FIG. 3.— Peak luminosity vs. decline time for HFF14Spo and assorted categories of explosive transients. Observed constraints of the HFF14Spo events are plotted as overlapping colored bands, along the left side of the figure. HFF14Spo-NW is shown as cyan and blue bands, corresponding to independent constraints drawn from the F435W and F814W light curves, respectively. For HFF14Spo-SE the scarlet and maroon bands show constraints from the F125W and F160W light curves, respectively. The width and height of these bands incorporates the uncertainty due to magnification (we adopt $10 < \mu < 100$) and the time of peak. In the top panel, ellipses and rectangles mark the luminosity and decline-time regions occupied by various explosive transient classes. Filled shapes show the empirical bounds for transients with a substantial sample of known events. Dashed regions mark theoretical expectations for rare transients that lack a significant sample size: the “Ia” class of white dwarf He shell detonations and the kilonova class from neutron star mergers. Grey bands in both panels show the MMRD relation for classical novae. In the lower panel, circles mark the observed peak luminosities and decline times for classical novae, while black ‘+’ symbols mark recurrent novae from our own galaxy. The large cross labeled at the bottom shows the rapid recurrence nova M31N 2008-12a. Each orange diamond marks a separate short transient event from the two rapid LBV outburst systems, SN 2009ip (Pastorello *et al.* 2013) and NGC3432-LBV1 (a.k.a. SN 2000ch Pastorello *et al.* 2010). These LBV events provide only upper limits on the decline time due to limited photometric sampling.

TABLE 1
LENS MODEL PREDICTIONS FOR TIME DELAYS AND MAGNIFICATIONS AT THE OBSERVED LOCATIONS OF THE HFF14Spo TRANSIENTS.

Model	$ \mu_{\text{NW}} $	$ \mu_{\text{SE}} $	$ \mu_{11.3} $	$\Delta t_{\text{NW:SE}}$ (days)	$\Delta t_{\text{NW:11.3}}$ (years)
CATS	196^{+140}_{-53}	46^{+2}_{-1}	$3.3^{+0.0}_{-0.0}$	$-1.7^{+2.0}_{-1.9}$	$-3.7^{+0.1}_{-0.2}$
GLAFIC	29^{+43}_{-10}	84^{+103}_{-38}	$3.0^{+0.2}_{-0.2}$	$4.1^{+5.5}_{-3.4}$	$-5.0^{+0.5}_{-0.6}$
GLEE	182^{+203}_{-83}	67^{+31}_{-16}	$2.9^{+0.1}_{-0.1}$	36^{+6}_{-7}	$-6.1^{+0.3}_{-0.2}$
GRALE	13^{+11}_{-6}	12^{+9}_{-5}	$3.1^{+2.2}_{-0.9}$	-10^{+1}_{-7}	$-2.5^{+1.0}_{-3.1}$
SWunited	38 ± 8	13 ± 1	2.9 ± 0.1
WSLAP ⁺	35 ± 20	30 ± 20	...	-48 ± 10	0.8
ZLTM	103^{+48}_{-40}	32^{+8}_{-10}	3.5 ± 0.3	43^{+12}_{-10}	-3.7 ± 0.3

NOTE. — Each lens model is identified by the name of the modeling method. Time delays give the predicted delay relative to an appearance in the NW host image, 11.2. Positive (negative) values indicate the NW image is the leading (trailing) image of the pair.

released by even the most extreme stellar flare falls far short of the observed energy release from the HFF14Spo transients (Balona 2012; Karoff *et al.* 2016).

We can also rule out active galactic nuclei (AGN), in which brief transient episodes (a few days in duration) may be observed from X-ray to infrared wavelengths (e.g. Gaskell and Klimek 2003), principally due to the quiescence of the HFF14Spo sources between the two observed episodes and the absence of any of the broad emission lines that are often (though not always) observed in AGN. No x-ray emitting point source was detected in 7 epochs of imaging from the Swift and Chandra x-ray space telescopes, collected from 2009 to 2014 (Methods 4.6). This includes the Chandra imaging on August 31, 2014 (MJD=56900), which was coeval with the peak of IR emission from HFF14Spo-SE, observed with *HST*.

Many types of stellar explosions can generate isolated transient events, and a useful starting point for classification of such objects is to examine their position in the phase space of peak luminosity versus decline time (see, e.g., Kulkarni *et al.* 2007). We have inferred a range of plausible luminosities and decline times for the HFF14Spo events using linear interpolation of the observed photometry (Methods 4.7), with corrections for the luminosity distance (assuming a standard Λ CDM cosmology), and accommodating the range of viable lensing magnifications ($10 < \mu < 100$) derived from the cluster lens models. This results in two-dimensional constraints on L_{pk} and the decline timescale t_2 (the time over which the transient declines by 2 magnitudes). The HFF14Spo-NW and HFF14Spo-SE events are largely consistent with each other, and if both events are representative of a single system (or a homogeneous class) then the most likely peak luminosity and decline time (the region with the most overlap) would be $L_{\text{pk}} \sim 10^{41}$ ergs/s and $t_2 \sim 1$ day.

As shown in Figure 3, the relatively low peak luminosities and the very rapid rise and fall of both HFF14Spo light curves are incompatible with all of the common categories of stellar explosions. This includes the thermonuclear explosions of white dwarf stars as Type Ia SNe, and the heterogeneous class of core collapse SNe.

Less well-understood classes are also ruled out, such as Superluminous SNe (Gal-Yam 2012; Arcavi *et al.* 2016), Type Iax SNe (Li *et al.* 2003; Jha *et al.* 2006; Foley *et al.* 2013), fast optical transients (Drout *et al.* 2014), Ca-rich SNe (Filippenko *et al.* 2003; Perets *et al.* 2011; Kasliwal *et al.* 2012), and Luminous Red Novae (also called intermediate luminosity red transients; Munari *et al.* 2002; Kulkarni *et al.* 2007; Kasliwal *et al.* 2011a).

The SN-like transients that come closest to matching the observed characteristics of the two HFF14Spo events are the “kilonova” class (also called a “macronova” or “mini-supernova”) and the “.Ia” class. Kilonovae are a theorized category of optical transients that may be generated by the merger of a neutron star (NS) binary. Such a NS+NS merger can drive a relativistic jet that may be observed as a Gamma Ray Burst (GRB) and would emit gravitational waves. These may also be accompanied by a very rapid optical light curve (the kilonova component) that is driven by the radioactive decay of r-process elements in the ejecta (Li and Paczyński 1998; Kulkarni 2005). The .Ia class is due to He shell explosions that are expected to arise from AM Canum Venaticorum (AM CVn) binary star systems undergoing He mass transfer onto a white dwarf primary star (Warner 1995; Nelemans and Tout 2005; Bildsten *et al.* 2007). The HFF14Spo light curves exhibited a slower rise time than is expected for a kilonova event (e.g., Metzger *et al.* 2010; Barnes and Kasen 2013; Kasen *et al.* 2015), and a faster decline time than is anticipated for a .Ia event (e.g., Shen *et al.* 2010). Furthermore, the HFF14Spo observations are not well matched by the few examples of observed kilonova candidates (Perley *et al.* 2009; Tanvir *et al.* 2013) or .Ia candidates (Kasliwal *et al.* 2010; Perets *et al.* 2010; Poznanski *et al.* 2010). However, there is enough uncertainty about the diversity of light curves generated by these rare explosions that we cannot dismiss these models on the basis of light curve characteristics alone.

In addition to the incompatibility of the light curve shape, another problem for all of the catastrophic stellar explosions discussed so far is that they cannot explain the appearance of *repeated* transient events. As shown in Table 1, none of the MACS0416 lens models predict an 8 month time delay between appearances in host galaxy images 11.1 and 11.2, suggesting that HFF14Spo-SE is not a time-delayed image of HFF14Spo-NW (as was the case for the 5th image of SN Refsdal; Kelly *et al.* 2015, 2016).

Neither the kilonova nor the .Ia explosion models can accommodate repeated events from the same source. The kilonova progenitor systems are completely disrupted at explosion. For .Ia events, even if an AM CVn system could produce repeated He shell flashes of similar luminosity, the period of recurrence would be of order 10^5 yr, making these effectively non-recurrent sources. Thus, to reconcile any cataclysmic explosion model with the two observed HFF14Spo events we would need to invoke a highly serendipitous occurrence of two unrelated peculiar explosions in the same host galaxy in the same year. This is not unheard of for common SN classes (e.g. Poznanski *et al.* 2009), but it is difficult to quantitatively assess the likelihood of such an occurrence for fainter rapid transients, as there are no measured rates of .Ia or kilonovae. In a study of very fast optical transients with the Pan-STARRS1 survey, Berger *et al.* (2013) derived a limit of

$\lesssim 0.05 \text{ Mpc}^{-3} \text{ yr}^{-1}$ for transients reaching $M \approx -14$ mag on a timescale of ~ 1 day. This limit, though several orders of magnitude higher than the constraints on novae or SNe, is sufficient to make it exceedingly unlikely that two unrelated fast optical transients would appear in the same galaxy in a single year. Furthermore, we have observed no other transient events with similar luminosities and light curve shapes in high-cadence surveys of 5 other Frontier Fields clusters. Indeed, all other transients detected in the primary HFF survey have been fully consistent with normal SNe. Thus, we have no evidence to suggest that transients of this kind are common enough to be observed twice in a single galaxy in a single year.

Although the two events were most likely not *temporally* coincident, all six lens models indicate that it is entirely plausible for the two HFF14Spo events to be *spatially* coincident: they can be mapped back to the same physical location at the source plane. This is supported by the fact that the host galaxy colors and spectral indices at each HFF14Spo location are indistinguishable within the uncertainties (Methods 4.8). Thus, to accommodate all of the observations of the HFF14Spo events with a single astrophysical source, we turn to two categories of stellar explosion that are sporadically recurrent: luminous blue variables (LBVs) and recurrent novae (RNe).

2.2. Luminous Blue Variable

The transient sources categorized as LBVs are the result of eruptions or explosive episodes from massive stars ($> 10M_{\odot}$). The class is exemplified by prototypical examples such as P Cygni, η Carinae (η Car), and S Doradus (S-Dor) (for recent overviews of the LBV class, see Smith *et al.* 2011; Kochanek *et al.* 2012). Although most giant LBV eruptions have been observed to last much longer than the HFF14Spo events (Smith *et al.* 2011), some LBVs have exhibited repeated rapid outbursts that are broadly consistent with the very fast HFF14Spo light curves (Methods 4.9). Because of this commonly seen stochastic variability, the LBV hypothesis does not have any trouble accounting for the HFF14Spo events as two separate episodes.

Two well-studied LBVs that provide a plausible match to the observed HFF14Spo events are “SN 2009ip” (Maza *et al.* 2009) and NGC3432-LBV1 (Pastorello *et al.* 2010). Both exhibited multiple brief transient episodes over a span of months to years (e.g., Miller *et al.* 2009; Li *et al.* 2009; Berger *et al.* 2009; Drake *et al.* 2010; Pastorello *et al.* 2010). Unfortunately, for these outbursts we have only upper limits on the decline timescale, t_2 , due to the relatively sparse photometric sampling. Figure 3b shows that both HFF14Spo events are consistent with the observed luminosities and decline times of these fast and bright LBV outbursts – though the HFF14Spo events would be among the most rapid and most luminous LBV eruptions ever seen.

In addition to those relatively short and very bright giant eruptions, most LBVs also commonly exhibit a slower underlying variability. P Cygni and η Car, for example, slowly rose and fell in brightness by ~ 1 to 2 mag over a timespan of several years before and after their historic giant eruptions. Such variation has not been detected at the HFF14Spo locations. Nevertheless, given the broad range of light curve behaviors seen in LBV events, we

cannot reject this class as a possible explanation for the HFF14Spo system.

To explore some of the physical implications of an LBV classification for the two HFF14Spo events, we first make a rough estimate of the total radiated energy, which can be computed using the decline timescale t_2 and the peak luminosity L_{pk} following Smith *et al.* (2011):

$$E_{\text{rad}} = \zeta t_2 L_{\text{pk}}, \quad (1)$$

where ζ is a factor of order unity that depends on the precise shape of the light curve.⁴³ Adopting $L_{\text{pk}} \sim 10^{41} \text{ erg s}^{-1}$ and $t_2 \sim 2$ days (as shown in Figure 3), we find that the total radiated energy is $E_{\text{rad}} \sim 10^{46} \text{ erg}$. A realistic range for this estimate would span $10^{44} < E_{\text{rad}} < 10^{47} \text{ erg}$, due to uncertainties in the magnification, bolometric luminosity correction, decline time, and light curve shape (in roughly that order of importance). These uncertainties notwithstanding, our crude estimate does fall well within the range of plausible values for the total radiated energy of a major LBV outburst.

The precise physical mechanism for LBV outbursts is still not fully understood (e.g. Smith and Owocki 2006; Woosley *et al.* 2007; Dessart *et al.* 2010), but the canonical model is that LBV transient events are the optical signature of an eruptive mass loss episode. If this applies to the HFF14Spo transients, then the energy budget must also include a substantial amount of kinetic energy imparted to the ejected gas shell. Without spectroscopic information from the HFF14Spo transients we cannot place any realistic estimate on the kinetic energy. Nevertheless, we can take the radiated energy as a rough lower limit on the total energy release and consider what timescale would be required for a massive star to build up that amount of energy (Methods 4.10). This approach assumes that the energy released in an LBV eruption is generated slowly in the stellar interior and is in some way “bottled up” by the stellar envelope, before being released in a rapid mass ejection. By assuming that the build-up timescale is comparable to the rest-frame time between the two observed events, we estimate a quiescent luminosity of $L_{\text{qui}} \sim 10^{39.5} \text{ erg s}^{-1}$ ($M_V \sim -10$). This value is fully consistent with the expected range for LBV progenitor stars (e.g., η Car has $M_V \sim -12$ and the faintest known LBV progenitors such as SN 2010dn have $M_V \sim -6$).

2.3. Recurrent Nova

Novae occur in binary systems in which a white dwarf star accretes matter from a less massive companion, leading to a burst of nuclear fusion in the accreted surface layer that causes the white dwarf to brighten by several orders of magnitude, but does not completely disrupt the star. In a recurrent nova (RN) system, the mass transfer from the companion to the white dwarf restarts after the explosion, so the cycle may begin again and repeat after a period of months or years.

The light curves of many RN systems in the Milky Way are similar in shape to the HFF14Spo episodes, exhibiting a sharp rise (< 10 days in the rest-frame) and a similarly rapid decline (see Methods section 4.11). This

⁴³ Note that Smith *et al.* (2011) used $t_{1.5}$ instead of t_2 , which amounts to a different light curve shape term, ζ .

is reflected in Figure 3, where novae are represented by a grey band that traces the empirical constraints on the maximum magnitude - rate of decline (MMRD) relation for classical novae (Della Valle and Livio 1995; Downes and Duerbeck 2000; Shafter *et al.* 2011; Kasliwal *et al.* 2011b).

The RN model can provide a natural explanation for having two separate explosions that are coincident in space but not in time, as the two observed HFF14Spo events can be attributed to two distinct eruptions from the same RN system. However, the recurrence timescale for HFF14Spo in the rest-frame is 120 ± 30 days, which would be a singularly rapid recurrence period for a RN system. All RNe in our own galaxy have recurrence timescales ranging from 15–80 years (Schaefer 2010). The fastest measured recurrence timescale belongs to M31N 2008a-12, which has exhibited a new outburst every year from 2009–2015 (Tang *et al.* 2014; Darnley *et al.* 2014, 2015; Henze *et al.* 2015a,b). Although this M31 record-holder demonstrates that very rapid recurrence is possible, classifying HFF14Spo as a RN would still require a very extreme mass transfer rate to accommodate the < 1 year recurrence. The non-detection of the HFF14Spo events in x-ray imaging from the Chandra space telescope (Methods 4.6) is also problematic for the RN hypothesis, as the optical emission of a nova is commonly followed by a supersoft x-ray phase that can last months to years (Hachisu and Kato 2006, e.g.).

Another major concern with the RN hypothesis is that the two HFF14Spo events are substantially brighter than all known novae – perhaps by as much as 2 orders of magnitude. One might attempt to reconcile the HFF14Spo luminosity more comfortably with the nova class by assuming a significant lensing magnification for one of the two events. This would drive down the intrinsic luminosity, perhaps to $\sim 10^{40} \text{ erg s}^{-1}$, on the edge of the nova region. However, this assumption implicitly moves the lensing critical curve to be closer to the HFF14Spo event in question. That pulls the critical curve away from the other HFF14Spo position, which makes that second event *more inconsistent* with observed nova peak luminosities.

The combination of a rapid recurrence timescale and unusually high peak luminosity for the HFF14Spo events is at odds with theoretical expectations and empirical constraints for RNe (see Methods section 4.12). Although the RN model is not strictly ruled out, we can deduce that if the HFF14Spo transients are caused by a single RN system, then that progenitor system would be the most extreme white dwarf binary system yet known.

2.4. Microlensing

In the presence of strong gravitational lensing it is possible to generate a transient event from lensing effects alone. In this case the background source has a steady luminosity but the relative motion of the source, lens, and observer causes the magnification of that source (and therefore the apparent brightness) to change rapidly with time. An isolated strong lensing event with a rapid timescale can be generated when a background star crosses over a lensing critical curve. In the case of a star crossing the caustic of a smooth lensing potential, the amplification of the source flux would increase (decrease) with a characteristic $t^{-1/2}$ profile as it moves

toward (away from) the caustic. This slowly evolving light curve then transitions to a very sharp decline (rise) when the star has moved to the other side of the caustic (Schneider and Weiss 1986; MiraldaEscude 1991). With a more complex lens comprising many compact objects, the light curve would exhibit a superposition of many such sharp peaks (Lewis *et al.* 1993).

The peculiar transient *Icarus*, observed behind the Hubble Frontier Fields cluster MACS J1149.6+2223, has been proposed as the first observed example of such a stellar caustic crossing event (P. Kelly *et al.*, in prep.). Kelly *et al.* find that such events may be expected to appear more frequently in strongly lensed galaxies that have small angular separation from the center of a massive cluster. In such a situation, our line of sight to the lensed background galaxy passes through a dense web of overlapping micro-lenses caused by the intracluster stars distributed around the center of the cluster. This has the effect of “blurring” the magnification profile across the cluster critical curve, making it more likely that a single (and rare) massive star in the background galaxy gets magnified by the required factor of $\sim 10^5$ to become visible as a transient caustic crossing event. On this basis the HFF14Spo host galaxy images are suitably positioned for caustic crossing transients, as they are seen through a relatively high density of intracluster stars—comparable to that observed for the *Icarus* transient (Methods 4.13).

The characteristic timescale of a canonical caustic crossing event would be on the order of hours or days (Methods 4.14), which is comparable to the timescales observed for the HFF14Spo events. Gravitational lensing is achromatic as long as the size of the source is consistent across the spectral energy distribution (SED). This means that the color of a caustic crossing transient will be roughly constant. Using simplistic linear interpolations of the observed light curves (Methods 4.7) we find that the inferred color curves for both HFF14Spo events are marginally consistent with this expectation of an unchanging color (Methods 4.15).

In the baseline lensing configuration adopted above—where a single critical curve subtends the HFF14Spo host galaxy arc—these events cannot plausibly be explained as stellar caustic crossings, because neither transient is close enough to the single critical curve to reach the required magnifications of $\mu \sim 10^6$. Some lens models can, however, be modified so that instead of just two host images, the lensed galaxy arc is made up of many more images of the host, with multiple critical curves subtending the arc where the HFF14Spo events appeared. By tuning the assumed masses of cluster galaxies near the HFF14Spo host, those multiple critical curves can be made to pass very close to the positions of the two HFF14Spo transient events. In the *Kawamata* and *Diego* lens models, this alternative lensing arrangement requires that the masses of the two nearest cluster galaxies are increased by 30 – 60%. With this adjustment, both models can reproduce the observed morphology of the HFF14Spo host galaxy as a smooth, unbroken arc. These model realizations imply magnifications on the order of $\mu \sim 1000$ for both HFF14Spo transients. If this alternative lensing situation is correct, then similar microlensing transients would be expected to appear at

different locations along the host galaxy arc, instigated by new caustic crossing episodes from different stars in the host galaxy.

3. DISCUSSION

We have examined three plausible explanations for the HFF14Spo events: (1) these transients are due to a RN that reaches an extraordinarily high peak luminosity, (2) they are separate rapid outbursts of an LBV star, or (3) they are each the result of the rapidly changing magnification of a massive star crossing over one or more lensing caustics. Our preferred explanation for the HFF14Spo events is that we have observed two distinct eruptive episodes from a massive LBV star. The light curve shape is consistent with rapid LBV eruptions seen in systems such as SN 2009ip and NGC 3432-LBV1. The peak luminosity and recurrence timescale are also within the bounds of what has been observed from nearby LBVs. The HFF14Spo episodes may have been among the fastest and most luminous of any rapid LBV events yet observed. However, the rapid outbursts of LBV stars in the local universe have never yet been observed with such a high cadence, so the detailed light curve shape of the HFF14Spo events cannot be rigorously compared against other events. In this scenario, the HFF14Spo LBV system would most likely have exhibited multiple eruptions over the last few years, but most of them were missed, as they landed within the large gaps of the *HST* Frontier Fields imaging program.

We speculate that the very luminous and very fast HFF14Spo transients may be driven by extreme mass eruption events or an extreme form of stellar pulsation. Both of these mechanisms are likely to occur in LBV progenitor stars, but there is not yet a consensus model that explains precisely how LBV eruptions are generated. This is a topic in need of significant theoretical work, with the end goal being a comprehensive physical model that accommodates both the η Car-like great eruptions and the S Dor-type variation of LBVs. The HFF14Spo events are extreme in several dimensions, and should add a useful benchmark for this theoretical challenge.

The authors thank Mario Livio and Laura Chomiuk for helpful discussion of this paper.

Financial support for this work was provided to SAR and OG by NASA through grant HST-GO-13386 from the Space Telescope Science Institute (STScI), which is operated by Associated Universities for Research in Astronomy, Inc. (AURA), under NASA contract NAS 5-26555. LLRW would like to thank Minnesota Supercomputing Institute at the University of Minnesota for providing resources and support. RK acknowledges support in part by World Premier International Research Center Initiative (WPI Initiative), MEXT, Japan, and JSPS KAKENHI Grant Number 26800093 and 15H05892. J.M.D acknowledges support of the projects AYA2015-64508-P (MINECO/FEDER, UE), AYA2012-39475-C02-01 and the consolider project CSD2010-00064 funded by the Ministerio de Economia y Competitividad. MJ was supported by the Science and Technology Facilities Council (grant number ST/L00075X/1) and used the DiRAC Data Centric system at Durham University, operated by the Institute for Computational

Cosmology on behalf of the STFC DiRAC HPC Facility (www.dirac.ac.uk). MJ was funded by BIS National E-infrastructure capital grant ST/K00042X/1, STFC capital grant ST/H008519/1, and STFC DiRAC Operations grant ST/K003267/1 and Durham University. DiRAC is part of the National E-Infrastructure. SHS thanks the Max Planck Society for support through the Max Planck Research Group.

4. METHODS

4.1. Discovery

The transient HFF14Spo was discovered in *HST* imaging collected as part of the Hubble Frontier Fields (HFF) survey (HST-PID:13496, PI:Lotz), a multi-cycle program observing 6 massive galaxy clusters and associated “blank sky” parallel fields. Several *HST* observing programs have provided additional observations supplementing the core HFF program. One of these is the FrontierSN program (HST-PID:13386, PI:Rodney), which aims to identify and study explosive transients found in the HFF and related programs. The FrontierSN team discovered HFF14Spo in two separate HFF observing campaigns on the galaxy cluster MACS0416. The first was an imaging campaign in January, 2014 during which the MACS0416 cluster field was observed in optical bands using the Advanced Camera for Surveys Wide Field Camera (ACS-WFC). The second concluded in August, 2014, and imaged the cluster with the infrared detector of *HST*’s Wide Field Camera 3 (WFC3-IR).

To discover transient sources, the FrontierSN team processes each new epoch of *HST* data through a difference imaging pipeline,⁴⁴ using archival *HST* images to provide reference images (templates) which are subtracted from the astrometrically registered HFF images. In the case of MACS0416, the templates were constructed from images collected as part of the Cluster Lensing And Supernova survey with Hubble (CLASH, HST-PID:12459, PI:Postman). The resulting difference images are visually inspected for new point sources, and any new transients of interest (primarily supernovae, SNe) are followed up with additional *HST* imaging or ground-based spectroscopic observations as needed. For a more complete description of the operations of the FrontierSN program, see Rodney *et al.* (2015).

4.2. Photometry

The follow-up observations for HFF14Spo included *HST* imaging observations in infrared and optical bands using the WFC3-IR and ACS-WFC detectors, respectively. Tables 4 and 5 present photometry of the HFF14Spo events from all available *HST* observations. The flux was measured on difference images, first using aperture photometry with a 0''.3 radius, and also by fitting with an empirical point spread function (PSF). The PSF model was defined using *HST* observations of the G2V standard star P330E, observed in a separate calibration program. A separate PSF model was defined for each filter, but owing to the long-term stability of the *HST* PSF we used the same model in all epochs. All of the aperture and PSF fitting photometry was carried out using the PythonPhot software package (Jones *et al.* 2015).⁴⁵

4.3. Host Galaxy Spectroscopy

Spectroscopy of the HFF14Spo host galaxy was collected using three instruments on the Very Large Telescope (VLT). Observations with the VLT’s X-shooter cross-dispersed echelle spectrograph (Vernet *et al.* 2011)

were taken on October 19th, 21st and 23rd, 2014 (Program 093.A-0667(A), PI: J. Hjorth) with the slit centered on the position of HFF14Spo-SE. The total integration time was 4.0 hours for the NIR arm of X-shooter, 3.6 hours for the VIS arm, and 3.9 hours for the UVB arm. The spectrum did not provide any detection of the transient source itself (as we will see below, it had already faded back to its quiescent state by that time). However, it did provide an unambiguous redshift for the host galaxy of $z = 1.0054 \pm 0.0002$ from $\text{H}\alpha$ and the O[II] doublet in data from the NIR and VIS arms, respectively. These line identifications are consistent with two measures of the photometric redshift of the host: $z = 1.00 \pm 0.02$ from the BPZ algorithm (Benítez 2000), and $z = 0.92 \pm 0.05$ from the EAZY program (Brammer *et al.* 2008). Both were derived from *HST* photometry of the host images 11.1 and 11.2, spanning 4350–16000 Å.

Additional VLT observations were collected using the Visible Multi-object Spectrograph (VIMOS Le Fèvre *et al.* 2003), as part of the CLASH-VLT large program (Program 186.A-0.798; P.I.: P. Rosati; Rosati *et al.* 2014)), which collected \sim 4000 reliable redshifts over 600 arcmin² in the MACS0416 field (Grillo *et al.* 2015; Balestra *et al.* 2016). These massively multi-object observations could potentially have provided confirmation of the redshift of the HFF14Spo host galaxy with separate spectral line identifications in each of the three host galaxy images. On the MACS0416 field this program collected 1 hr of useful exposure time in good seeing conditions with the Low Resolution Blue grism. Unfortunately, the wavelength range of this grism (3600–6700 Å) does not include any strong emission lines for a source at $z=1.0054$, and the signal-to-noise (S/N) was not sufficient to provide any clear line identifications for the three images of the HFF14Spo host galaxy.

The VLT Multi Unit Spectroscopic Explorer (MUSE; Henault *et al.* 2003; Bacon *et al.* 2012) observed the NE portion of the MACS0416 field—where the HFF14Spo host images are located—in December, 2014 for 2 hours of integration time (ESO program 094.A-0115, PI: J. Richard). These observations also confirmed the redshift of the host galaxy with clear detection of the O[II] doublet. Importantly, since MUSE is an integral field spectrograph, these observations also provided a confirmation of the redshift of the third image of the host galaxy, 11.3, with a matching O[II] line at the same wavelength (Caminha *et al.* 2017, Richard *et al.* in prep).

A final source of spectroscopic information relevant to HFF14Spo is the Grism Lens Amplified Survey from Space (GLASS; PID: HST-GO-13459; PI:T. Treu; Schmidt *et al.* 2014; Treu *et al.* 2015). The GLASS program collected slitless spectroscopy on the MACS0416 field using the WFC3-IR G102 and G141 grisms on *HST*, deriving redshifts for galaxies down to a magnitude limit $H < 23$. As with the VLT VIMOS data, the three sources identified as images of the HFF14Spo host galaxy are too faint in the GLASS data to provide any useful line identifications. There are also no other sources in the GLASS redshift catalog⁴⁶ that have a spectroscopic redshift consistent with $z=1.0054$.

⁴⁴ <https://github.com/srodney/sndrizpipe>

⁴⁵ <https://github.com/djones1040/PythonPhot>

⁴⁶ <http://glass.astro.ucla.edu/>

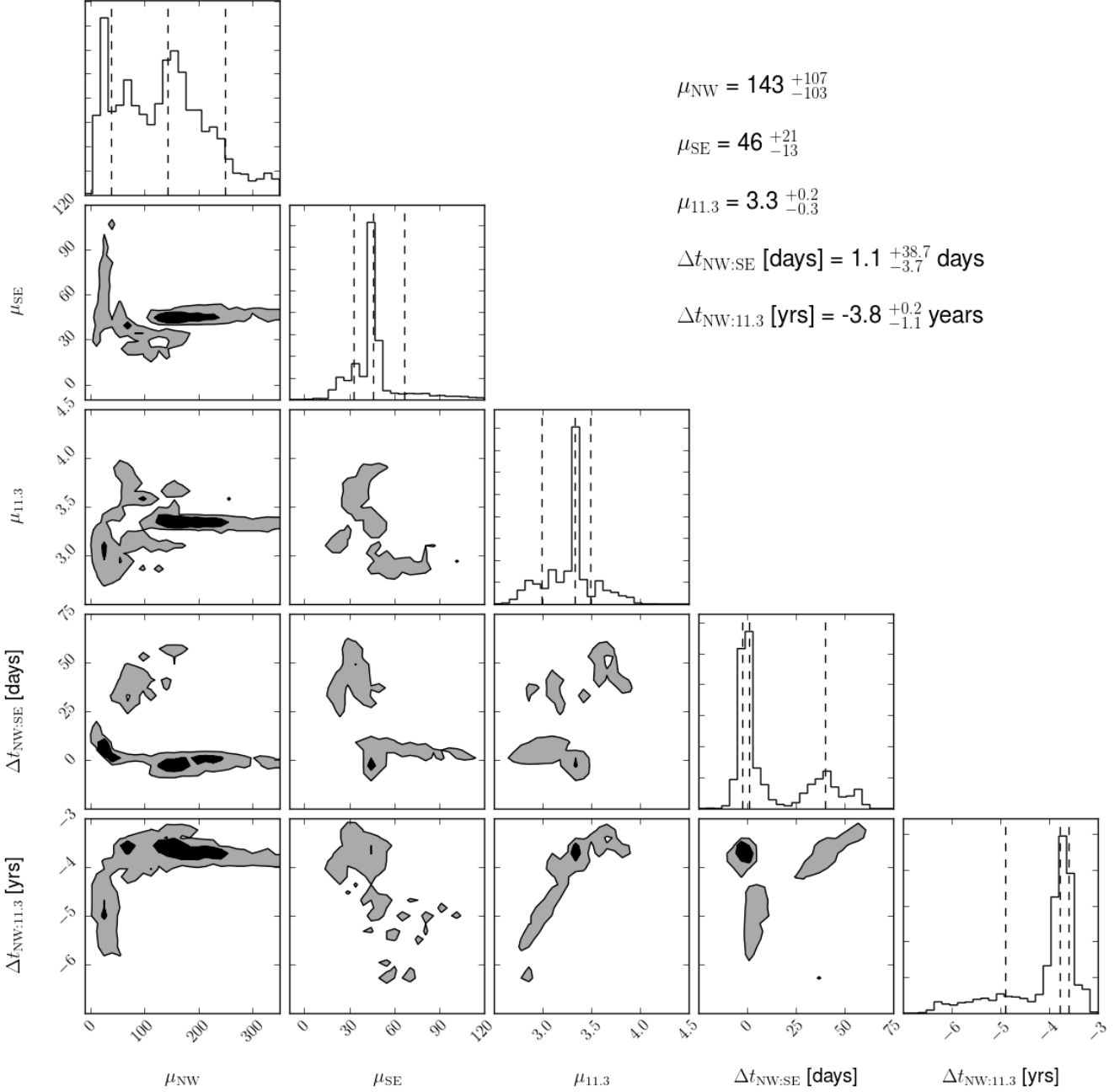


FIG. 4.— Probability distributions for the five primary magnification and time delay observables, drawn from a combination of results from five of our seven baseline lens models: CATS, GLAFIC, GLEE, GRALE, and ZLT. Contours shown in the ten panels at the lower left mark the $1-\sigma$ and $2-\sigma$ confidence regions in each two-dimensional slice of the parameter space. Histograms at the top of each column show the marginalized one-dimensional probability distributions, with dashed vertical lines marking the mean and 1σ confidence region. These mean values and uncertainties are also reported in the table of values at the upper right.

4.4. Gravitational Lens Models

The seven lens models used to provide estimates of the plausible range of magnifications and time delays are:

- **CATS:** The model of Jauzac *et al.* (2014), generated with the **LENSTOOL** software (Jullo *et al.*

2007),⁴⁷ using strong lensing constraints. This model makes a light-traces-mass assumption and parameterizes cluster and galaxy components using pseudo-isothermal elliptical mass distribution (PIEMD) density profiles (Elíasdóttir *et al.* 2007; Limousin *et al.* 2007).

⁴⁷ <http://projects.lam.fr/repos/lenstool/wiki>

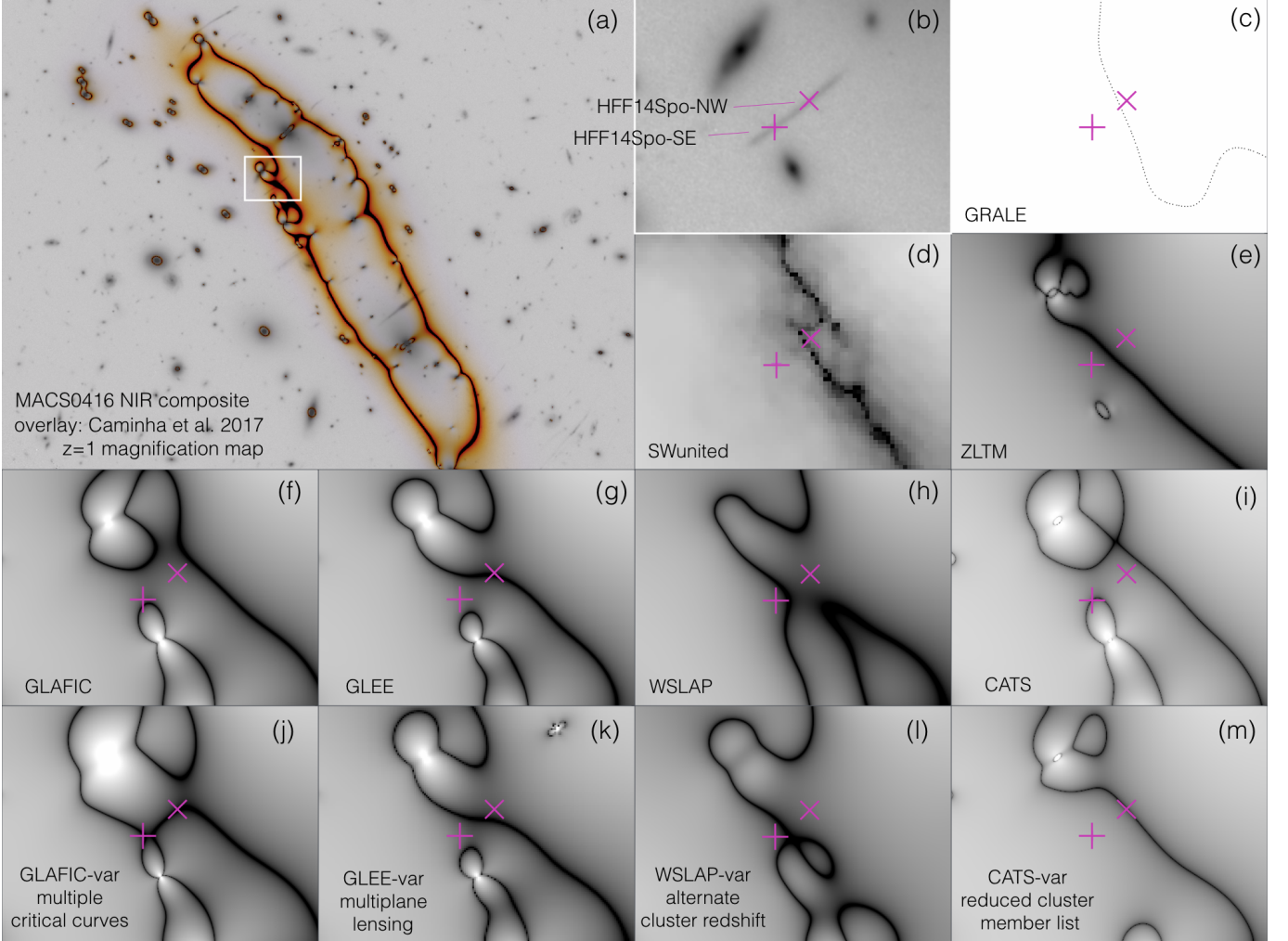


FIG. 5.— Locations of the lensing critical curves relative to the positions of the two HFF14Spo sources. Panel (a) shows the HST Frontier Fields composite near-infrared image of the full MACS0416 field. The magnification map from the Caminha *et al.* (2017) model is overlaid with orange and black contours. The white box is shown in panel (b) with a closer view of the HFF14Spo host galaxy. Panels b shows a trace of the lensing critical curve from the GRALE model, and panels d-i show magnification maps for the six other primary models, all for a source at the HFF14Spo redshift. The magnification maps are plotted with log scaling, such that white is $\mu = 1$ and black is $\mu = 10^3$. Panels j-m show the same magnification maps, extracted from the lens model variations described in 4.5.

- **GLAFIC:** The model of Kawamata *et al.* (2016), built using the **GLAFIC**⁴⁸ software (Oguri 2010) with strong-lensing constraints. This model assumes simply parametrized mass distributions, and model parameters are constrained using positions of more than 100 multiple images.
- **GLEE:** A new model built using the **GLEE** software (Suyu and Halkola 2010; Suyu *et al.* 2012) with the same strong-lensing constraints used in Caminha *et al.* (2017), representing mass distributions with simply parameterized NFW profiles.
- **GRALE:** A free-form, adaptive grid model developed using the GRALE software tool (Liesenborgs *et al.* 2006, 2007; Mohammed *et al.* 2014; Sebesta *et al.* 2016), which implements a genetic algorithm to reconstruct the cluster mass distribution with projected Plummer 1911 density profiles.
- **SWUnited:** The model of Hoag *et al.* (2016), built using the **SWUnited** modeling method (Bradač *et al.* 2005, 2009), in which an adaptive pixelated grid iteratively adapts the mass distribution to match both strong- and weak-lensing constraints. Time delay predictions are not available for this model.
- **WSLAP+:** Created with the **WSLAP+** software (Sendra *et al.* 2014): Weak and Strong Lensing Analysis Package plus member galaxies (Note: no weak-lensing constraints used for this MACS0416 model). Interactive online model exploration available at <http://www.ifca.unican.es/users/jdiego/LensExplorer>.
- **ZLTM:** A model with strong- and weak-lensing constraints, built using the “light-traces-mass” (LTM) methodology (Zitrin *et al.* 2009, 2015), first presented for MACS0416 in Zitrin *et al.* (2013).

⁴⁸ <http://www.slac.stanford.edu/~oguri/glafic/>

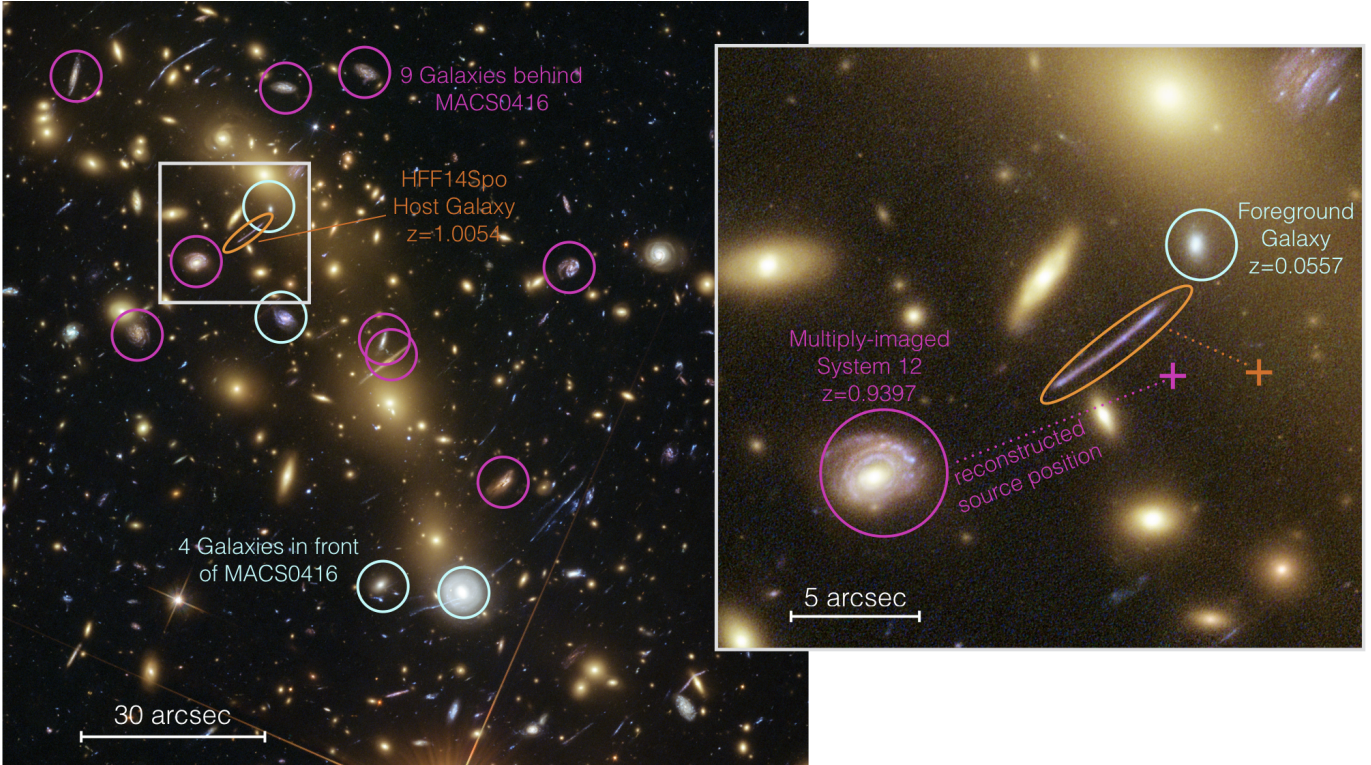


FIG. 6.— Galaxies in the foreground and background of the MACS0416 cluster that are included in the GLEE-var model, which is a variation of the GLEE model that accommodates multi-plane lensing. The larger panel at left marks nine galaxies with spectroscopic redshifts greater than the cluster redshift (magenta circles) and four galaxies in the cluster foreground (light blue circles). The inset panel at right zooms in on the HFF14Spo host galaxy (enclosed by the orange ellipse in each panel). The magenta circle marks a spiral galaxy at $z = 0.9397$, which is also strongly lensed by the MACS0416 cluster into three highly distorted images (System 12 in Caminha *et al.* (2017)). The galaxy in the foreground of the cluster at $z = 0.0557$ is encircled in light blue. Crosses mark the reconstructed source positions (from the GLEE model) for the $z = 0.9397$ galaxy and the HFF14Spo host.

Early versions of the *SWUnited*, *CATS*, *ZLTM* and *GRALE* models were originally distributed as part of the Hubble Frontier Fields lens modeling project,⁴⁹ in which models were generated based on data available before the start of the HFF observations to enable rapid early investigations of lensed sources. The versions of these models applied here are updated to incorporate additional lensing constraints. In all cases the lens modelers made use of strong-lensing constraints (multiply-imaged systems and arcs) derived from *HST* imaging collected as part of the CLASH program (PI:Postman, HST-PID:12459, Postman *et al.* 2012). These models also made use of spectroscopic redshifts in the cluster field from Mann and Ebeling (2012), Christensen *et al.* (2012), Grillo *et al.* (2015) and Caminha *et al.* (2017). Input weak-lensing constraints were derived from data collected at the Subaru Telescope by PI K. Umetsu (in prep) and archival imaging.

Figure 4 presents probability distributions derived from these models for the three magnifications and two time delay values of interest. These distributions were derived by combining the Monte Carlo chains from the *CATS*, *GLAFIC*, *GLEE*, *GRALE* and *ZLTM* models, with weighting applied to account for the different number of model iterations in each chain. All five of these models agree that host image 11.3 is the leading image,

appearing some 3–7 years before the other two images. The models do not agree on the arrival sequence of images 11.1 and 11.2: some have the NW image 11.2 as a leading image, and others have it as a trailing image. However, the models do consistently predict that the separation in time between those two images should be roughly in the range of 1 to 60 days. As shown in Figure 7, HFF14Spo-NW and HFF14Spo-SE are inconsistent with these predicted time delays if one assumes that they are delayed images of a single event. However, if these were independent events, then a time delay on the order of tens of days between image 11.1 and 11.2 could have resulted in time-delayed events that were missed by the *HST* imaging of this field.

Because of the proximity of the critical curves in all models, the predicted time delays and magnification factors are significantly different if calculated at the model-predicted positions instead of the observed positions. For example, in the GLEE model series (GLEE-A and GLEE-B) when switching from the observed to model-predicted positions the arrival order of the NW and SE images flips, the expected time delay drops from tens of days to <1 day, and the magnifications decrease by 40–60%. However, the expected magnifications and time delays between the events still fall within the broad ranges summarized in Table 1 and shown in Figure 4. Regardless of whether the model predictions are extracted at the observed or predicted positions of the HFF14Spo events,

⁴⁹ For more details, see <https://archive.stsci.edu/prepds/frontier/lensmodels/>

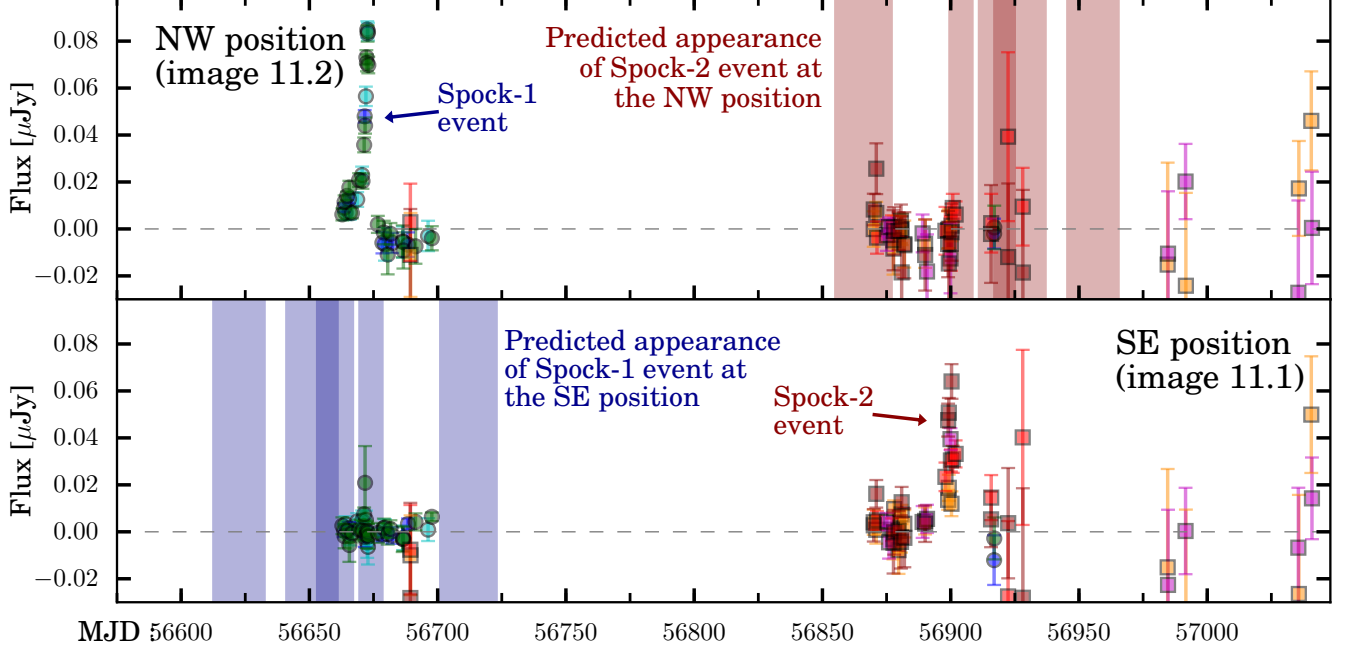


FIG. 7.— Predictions for the reappearance episodes of both HFF14Spo-NW and HFF14Spo-SE due to gravitational lensing time delays, as listed in Table 1. The top panel shows photometry collected at the NW position (host galaxy image 11.2) where the first event (HFF14Spo-NW) appeared in January, 2014. Optical measurements from ACS are in blue and green, and infrared observations from WFC3-IR are in red and orange, as in Figure 2. Each blue bar in the lower panel shows one lens model prediction for the dates when that same physical event (HFF14Spo-NW) would have also appeared in the SE location (galaxy image 11.1), due to gravitational lensing time delay. The lower panel plots photometry from the SE position (11.1). On the right side we see the second observed event (HFF14Spo-SE). The red bars above show model predictions for when the NW host image 11.2 would have exhibited the gravitationally delayed image of the HFF14Spo-SE event. The width of each bar encompasses the 68% confidence region for a single model, and darker regions indicate an overlap from multiple models.

none of the lens models can accommodate the observed 220-day time difference as purely a gravitational lensing time delay.

4.5. Lens Model Variations

We used variations of several lens models to investigate how the lensing critical curves shift under a range of alternative assumptions or input constraints. These variations highlight the range of systematic effects that might impact the model predictions for the HFF14Spo magnifications, time delays and proximity to the critical curves. Figure 5 shows the critical curves for a source at $z = 1$ (the redshift of the HFF14Spo host galaxy) predicted by our seven baseline models, plus the four variations described below.

The baseline CATS model reported in Table 1 corresponds to the CATSv4.1 model published on the STScI Frontier Fields lens model repository⁵⁰. That model uses 178 cluster member galaxies, including a galaxy <5 arcsec south of the HFF14Spo host galaxy, which creates a local critical curve that intersects the HFF14Spo-SE location. Our CATS-var model is an earlier iteration of the model, published on the STScI repository as CATSv4⁵¹, and includes only 98 galaxies identified as cluster members. In this variation the nearby cluster member galaxy

is not included, so the HFF14Spo-SE event is not intersected by a critical curve. However, the HFF14Spo-NW event is approximately coincident with a the primary critical curve of the MACS0416 cluster. When the critical curve is close to either HFF14Spo location, the magnifications predicted by the CATS model are driven up to $\mu > 100$. However, the time delays remain small, on the order of tens of days, and incompatible with the observed 220-day gap.

The WSLAP-var model evaluates whether the cluster redshift significantly impacts the positioning of the critical curve. In this merging cluster, the northern brightest cluster galaxy (BCG) has a slightly higher redshift than the southern BCG. The mean redshift of the cluster is not precisely determined, since it is likely to be aligned somewhat along the line of sight. For the WSLAP-var model we shift the assumed cluster redshift $z = 0.4$ from the default $z = 0.396$ (used in all the baseline models). The shift in the critical curve is noticeable, but not substantial, insofar as this change does not drive the critical curve to intersect either or both of the HFF14Spo locations.

The GLEE-var model is a multi-plane lens model that incorporates 13 galaxies with spectroscopic redshifts that place them either in the foreground or background of the MACS0416 cluster. Figure 6 marks these 13 galaxies and highlights two of them that appear in the foreground of the HFF14Spo host galaxy and are close to the lines of sight to the HFF14Spo transients. Both the foreground

⁵⁰ <https://archive.stsci.edu/pub/hlsp/frontier/macs0416/models/cats/v4.1/>

⁵¹ <https://archive.stsci.edu/pub/hlsp/frontier/macs0416/models/cats/v4/>

$z = 0.0557$ galaxy and the reconstructed position of the $z = 0.9397$ galaxy have a projected separation of $< 4''$ from the HFF14Spo-SE transient position. Including these galaxies in the GLEE lensing model has a minor impact on the magnifications and time delays, and also results in a shift of the position of the critical curve—as can be seen by comparing the GLEE-A and GLEE-B models in Figure 5. For the GLEE model, incorporating these line-of-sight effects does not substantially change the predicted magnifications or time delays, and the predicted time delays are still incompatible with the observed gap of 220 days between events.

The GLAFIC-var model examines whether it is plausible for a critical curve to intersect both HFF14Spo locations—contrary to the baseline assumption of a single critical curve subtending the HFF14Spo host galaxy roughly midway between the two positions. This model includes a customized constraint, requiring that the magnification factors at the HFF14Spo positons are > 1000 . To achieve this, we independently adjusted the mass scaling for the two nearest cluster member galaxies, which are located just northeast and south of the HFF14Spo host galaxy arc. The mass of the northeast member galaxy was increased by $\sim 30\%$ and that of the southern one by $\sim 60\%$. As a simple check of the predicted morphology of the host galaxy, we placed a source with a simple Sérsic (1963) profile on the source plane. The lensed image of that artificial source is an unbroken elongated arc, reproducing the host galaxy image morphology reasonably well.

For this modification of the GLAFIC lens model to be justified in a statistical sense, the revised model should still accurately reproduce the observed strong-lensing constraints across the entire cluster. The χ^2 statistic for the baseline GLAFIC model is 240, with 196 degrees of freedom ($\chi^2_\nu = 1.2$), and yields an Akaike information criterion (AIC) (Akaike 1974) of 676. For the GLAFIC-var model that forces multiple critical curves to intersect the HFF14Spo locations, we get $\chi^2 = 331$ for 192 degrees of freedom ($\chi^2_\nu = 1.7$) and AIC=769. This suggests that the multiple critical curve GLAFIC-var model is strongly disfavored by the *positional* strong-lensing constraints that are used for both models. However, we note that neither model incorporates the temporal constraints of the observed time delay.

4.6. X-ray Non-detections

The MACS0416 field was observed by the SWIFT X-Ray Telescope (XRT) and UltraViolet/Optical Telescope (UVOT) in April 2013. No source was detected near the locations of the HFF14Spo events (N. Gehrels, private communication). The field was also observed by the Chandra X-ray space telescope with the ACIS-I instrument for three separate programs. On June 7, 2009 it was observed for GO program 10800770 (PI: H. Ebeling). It was revisited for GTO program 15800052 (PI: S. Murray) on November 20, 2013 and for GO program 15800858 (PI: C. Jones) on June 9, August 31, November 26, and December 17, 2014. These Chandra images show no evidence for an x-ray emitting point source near the HFF14Spo locations on those dates (S. Murray, private communication).

4.7. Light Curve Fitting

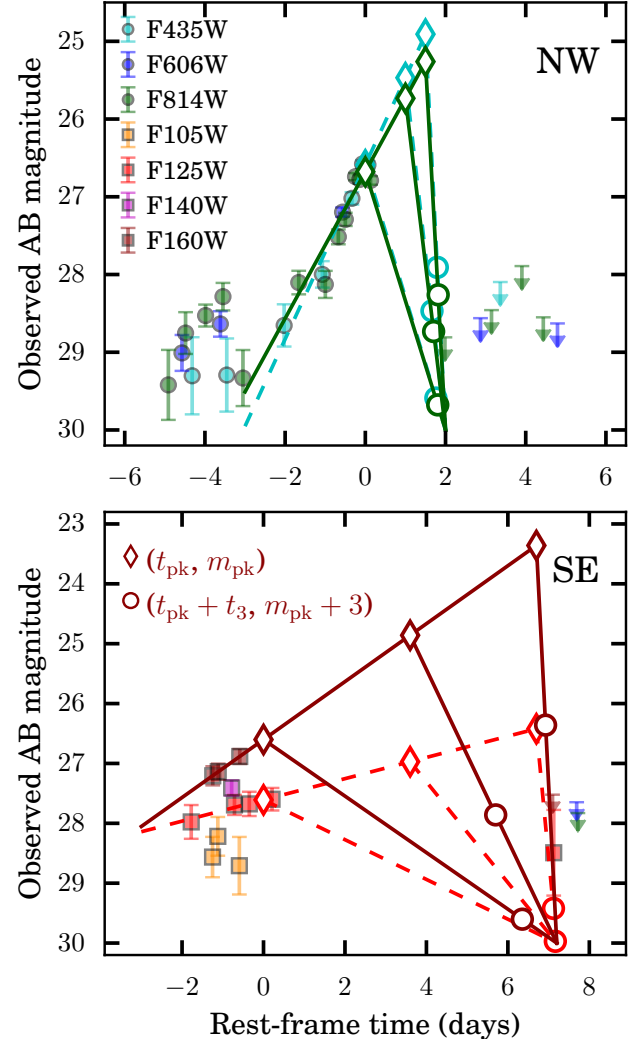


FIG. 8.— Piece-wise linear fits to the HFF14Spo light curves, used to measure the rise time and decay time of the two events. The HFF14Spo-NW light curve is shown in the top panel, and HFF14Spo-SE in the bottom. Filled points with error bars plot the observed brightness of each event in AB magnitudes as a function of rest-frame time (for $z = 1.0054$). Piece-wise linear fits are shown for the four bands that have enough points for fitting: in the top panel fits are plotted for the F814W band (solid green lines) and the F435W band (dashed cyan lines), while in the bottom panel fits are shown for F160W (solid maroon) and F125W (dashed scarlet). Open diamonds in each panel show three examples of assumptions for the time of peak brightness, t_{pk} (i.e. the position where the rising piece of the linear fit ends). Open circles mark the corresponding point, $t_{\text{pk}} + t_3$, at which the fading transient would have declined in brightness by 3 magnitudes. See text for details on the fitting procedure.

Due to the rapid decline timescale, no observations were collected for either event that unambiguously show the declining portion of the light curve. Therefore, we must make some assumptions for the shape of the light curve in order to quantify the peak luminosity and the corresponding timescales for the rise and the decline. We first approach this with a simplistic model that is piecewise linear in magnitude vs time. Figure 8 shows examples of the resulting fits for the two events. For each

fit we use only the data collected within 3 days of the brightest observed magnitude, which allows us to fit a linear rise separately for the F606W and F814W light curves for HFF14Spo-NW and the F125W and F160W light curves for HFF14Spo-SE. To quantify the covariance between the true peak brightness, the rise time and the decline timescale, we use the following procedure:

1. make an assumption for the date of peak, t_{pk} ;
2. measure the peak magnitude at t_{pk} from the linear fit to the rising light curve data;
3. assume the source reaches a minimum brightness (maximum magnitude) of 30 AB mag at the epoch of first observation after the peak;
4. draw a line for the declining light curve between the assumed peak and the assumed minimum brightness;
5. use that declining light curve line to measure the timescale for the event to drop by 2 magnitudes, t_2 ;
6. make a new assumption for t_{pk} and repeat.

As shown in Figure 8, the resulting piece-wise linear fits are simplistic, but nevertheless approximately capture the observed behavior for both events. Furthermore, since this toy model is not physically motivated, it allows us to remain agnostic for the time being as to the astrophysical source(s) driving these transients. From these fits we can see that HFF14Spo-NW most likely reached a peak magnitude between 25 and 26.5 AB mag in both F814W and F435W, and had a decline timescale t_2 of less than 2 days in the rest-frame. The observations of HFF14Spo-SE provide less stringent constraints, but we see that it had a peak magnitude between 23 and 26.5 AB mag in F160W and exhibited a decline time of less than seven days. These fits also illustrate the generic fact that a higher peak brightness corresponds to a longer rise time and a faster decline timescale, independent of the specific model used. Changes to the arbitrary constraints we placed on these linear fits do not substantially affect these results.

At any assumed value for the time of peak brightness this linear interpolation gives an estimate of the peak magnitude. We then convert that to a luminosity (e.g., νL_ν in erg s $^{-1}$) by first correcting for the luminosity distance assuming a standard Λ CDM cosmology, and then accounting for an assumed lensing magnification, μ . The range of plausible lensing magnifications ($10 < \mu < 100$) is derived from the union of our six independent lens models (Methods, Figure 4). This results in a grid of possible peak luminosities for each event as a function of magnification and time of peak. As we are using linear light curve fits, the assumed time of peak is equivalent to an assumption for the decline time, which we quantify as t_2 , the time over which the transient declines by 2 magnitudes.

4.8. Host Galaxy

To examine whether the two transients originated from the same physical location in the source plane, we looked

TABLE 2
PROPERTIES OF THE LOCAL STELLAR POPULATION IN THE HFF14SPO HOST GALAXY, FROM SED FITTING.

Host image:	11.1	11.2	11.3
Location:	HFF14Spo-SE	HFF14Spo-NW	center
$(U - V)_{\text{rest}}$	$0.69^{+0.2}_{-0.05}$	$0.52^{+0.15}_{-0.10}$	0.39 ± 0.05
$\log[\Sigma(M_*/\text{M}_\odot)]$	7.14 ± 0.15	7.14 ± 0.15	7.04 ± 0.10
Age (Gyr)	0.292 ± 0.5	0.290 ± 0.5	0.292 ± 0.5

for differences in the properties of the HFF14Spo host galaxy at the location of each event. We first used the technique of “pixel-by-pixel” SED fitting as described in Hemmati *et al.* (2014) to determine rest-frame colors and stellar properties in a single resolution element of the *HST* imaging data. For this purpose we used the deepest possible stacks of *HST* images, comprising all available data except those images where the transient events were present. The resulting maps of stellar population properties are shown in Figure 9. Table 2 reports measurements of the three derived stellar population properties (color, mass, age) from host images 11.1, 11.2 and 11.3. In 11.1 and 11.2 these measurements were extracted from the central pixel at the location of each of the two HFF14Spo events. The lensing magnification here ranges from $\mu = 10$ to 100 (see Section 4.4), corresponding to a size on the source plane between 6 and 600 pc 2 . For host image 11.3 we report the stellar population properties derived from the pixel at the center of the galaxy, because the lens models do not have sufficient precision to map the HFF14Spo locations to specific positions in image 11.3. With a magnification of ~ 3 to 5, this extraction region covers roughly 2000 to 6000 pc 2 .

The reported uncertainties for these derived stellar properties in Table 2 reflect only the measurement errors from the SED fitting, and do not attempt to quantify potential systematic biases. Such biases could arise, for example, from color differences in the background light, which is dominated by the cluster galaxies and varies significantly across the MACS0416 field. Such a bias might shift the absolute values of the parameter scales for any given host image (e.g., making the galaxy as a whole appear bluer, more massive and younger). However, the gradients across any single host image are unlikely to be driven primarily by such systematics.

Figure 9 and Table 2 show that the measured values of the color, stellar mass, and age at the two HFF14Spo locations are mutually consistent. Thus, it is plausible to assume that the two positions map back to the same physical location at the source plane. Comparing those two locations to the center of the galaxy as defined in image 11.3, we see only a mild tension in the rest-frame U-V color. This comparison therefore cannot quantitatively rule out the possibility that the two transient events are located at the center of the galaxy. However, the maps shown in Figure 9 do show a gradient in both U-V color and stellar age. For both images 11.1 and 11.2 the bluest and youngest stars ($U - V \sim 0.3$, $\tau \sim 280$ Myr) are localized in knots near the extreme ends of each image, well separated from either of the HFF14Spo transient events. In the less distorted host image 11.3 the bluer and younger stars are concentrated near the center. Taken together, these color and age gradients suggest that the two tran-

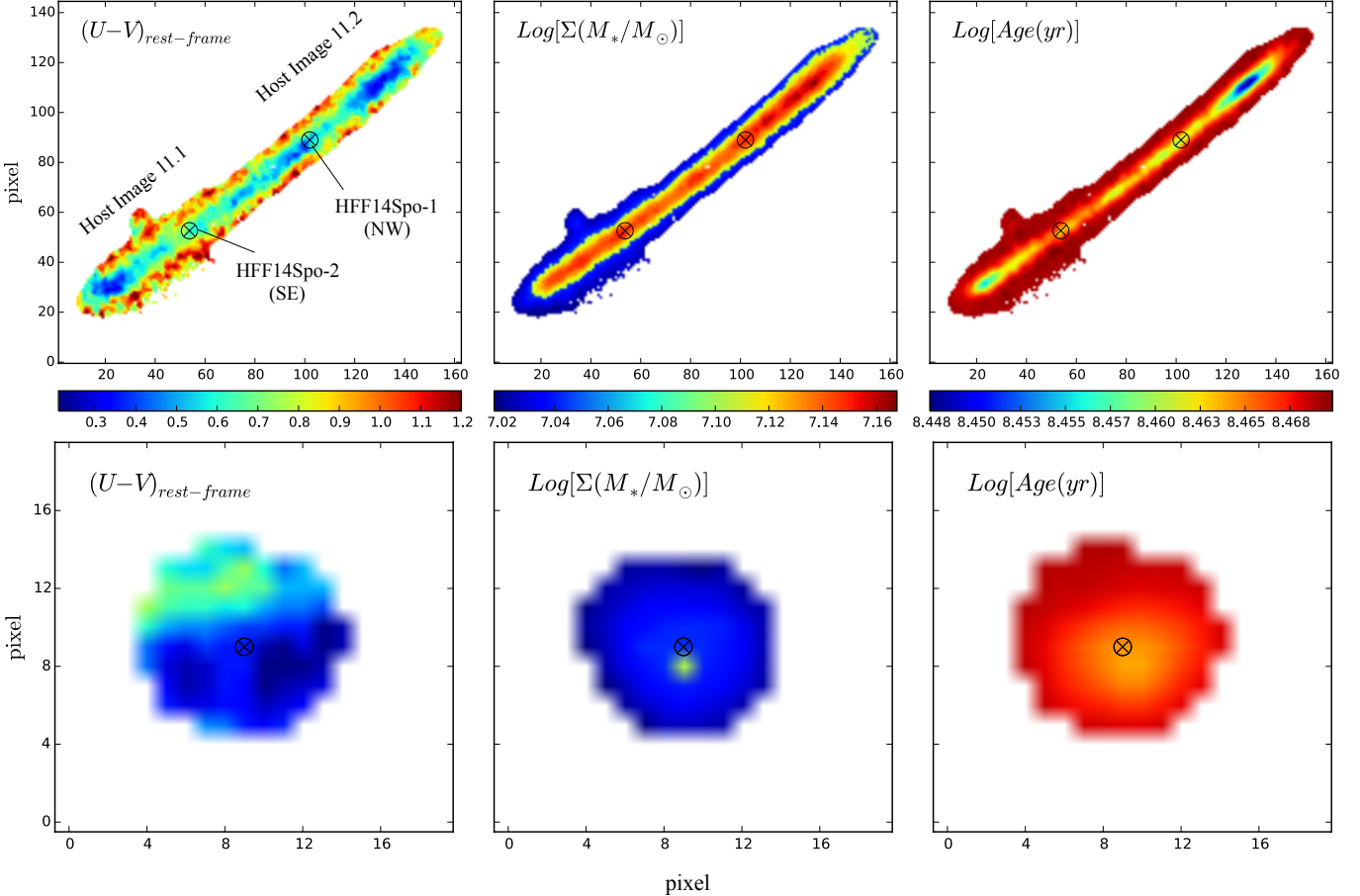


FIG. 9.— Stellar population properties of the HFF14Spo host galaxy, derived from “pixel-by-pixel” SED fitting. The top row shows maps for the adjacent host images 11.1 and 11.2, and the bottom panels show image 11.3. From left to right the panels present the rest-frame (U-V) color, the stellar surface mass density, Σ , and the mean age of the stellar population in Gyr. Markers in the top row denote the positions of the two HFF14Spo transient events. Markers in the bottom panels are at the center of host image 11.3.

sients are not coincident with the center of their host galaxy.

In addition to the *HST* imaging data, we also have spatially resolved spectroscopy from the MUSE integral field data. The only significant spectral line feature for the HFF14Spo host is the O[II] ($\lambda\lambda$ 3727, 3729) doublet, observed at 7474 and 7478 Å. Figure 10 shows the observed O[II] lines at 10 positions along the length of the arc, which comprises images 11.1 and 11.2. At each position the lines were extracted using apertures with a radius of 0''.6, so adjacent extractions are not independent, but extractions at the two HFF14Spo locations have no overlap. Each extraction has been normalized to show a peak line flux at unity, so that the line profiles and the doublet line ratios may be more easily compared.

Properties derived from these line fits are reported in Table 3. The O[II] lines do not exhibit any discernible gradient across the host galaxy images in terms of the wavelength of line centers, full width at half maximum, or the intensity ratio of the two components of the doublet. Thus, the O[II] measurements from MUSE cannot be used to distinguish either HFF14Spo location from the other, or to definitively answer whether either position is coincident with the center of the host galaxy. We conclude that it is plausible but not certain that the two

HFF14Spo events arose from the same physical location in the host galaxy.

4.9. Luminous Blue Variable Light Curve Comparison

Figure 11 presents a direct comparison of the observed HFF14Spo light curves against the light curves of the two LBVs that have well-studied rapid eruptions: SN 2009ip and NGC3432-LBV1. The brief outbursts of these LBVs have been less finely sampled than the two HFF14Spo events, but the available data show a wide variety of rise and decline times, even for a single object over a relatively narrow time window of a few months.

4.10. LBV Build-up timescale

The “build-up” timescale (Smith *et al.* 2011) matches the radiative energy released in an LBV eruption event with the radiative energy produced during the intervening quiescent phase:

$$t_{\text{rad}} = \frac{E_{\text{rad}}}{L_{\text{qui}}} = t_2 \frac{\xi L_{\text{pk}}}{L_{\text{qui}}}, \quad (2)$$

where L_{qui} is the luminosity of the LBV progenitor star during quiescence.

The HFF14Spo events are not resolved as individual stars in their quiescent phase, so we have no useful con-

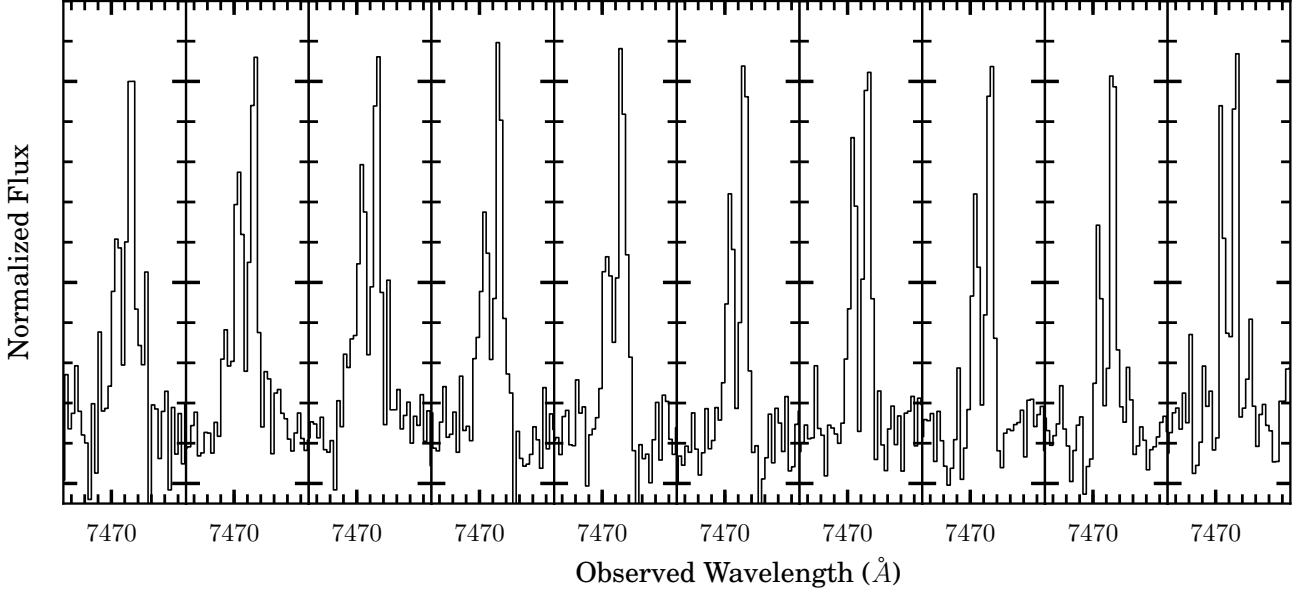


FIG. 10.— The [OII] line, observed with MUSE, at a series of ten locations along the HFF14Spo host galaxy arc. **TODO:** add in values for the [OII] doublet line ratio **TODO:** Add in panels showing [OII] lines from 11.3 and the spock locations. **TODO:** add in a panel showing the extraction apertures.

TABLE 3
MEASUREMENTS OF THE O[II] $\lambda\lambda 3626, 3629$ LINES FROM HFF14SPO HOST GALAXY IMAGES 11.1 AND 11.2^a

Aperture ID	R.A. J2000 (degrees)	Dec. J2000 (degrees)	distance to HFF14Spo-SE (Arcsec)	O[II] Flux ($\text{erg s}^{-1} \text{cm}^{-2}$)	λ_{center} (Å)	FWHM (Å)	O[II] Flux ($\text{erg s}^{-1} \text{cm}^{-2}$)	λ_{center} (Å)	FWHM (Å)	Line Ratio
1	64.039371	-24.070450	-1.54	2.19e-18	7472.37	4.00	3.57e-18	7478.17	4.00	1.63
2	64.039218	-24.070345	-0.88	4.73e-18	7472.16	4.00	5.30e-18	7478.12	3.40	1.12
3	64.039078	-24.070264	-0.30	5.05e-18	7472.29	4.00	6.10e-18	7478.27	3.73	1.21
4	64.038921	-24.070163	0.39	4.22e-18	7472.19	4.00	5.74e-18	7478.08	3.59	1.36
5	64.038785	-24.070078	0.97	3.86e-18	7472.25	4.00	6.56e-18	7478.19	4.00	1.70
6	64.038637	-24.069958	1.65	4.80e-18	7472.51	4.00	5.42e-18	7478.07	2.69	1.13
7	64.038501	-24.069865	2.24	4.60e-18	7472.57	3.43	5.74e-18	7478.17	3.20	1.25
8	64.038352	-24.069752	2.92	4.70e-18	7472.54	3.54	6.22e-18	7478.16	2.95	1.32
9	64.038229	-24.069648	3.50	3.26e-18	7472.83	2.80	5.79e-18	7478.16	2.84	1.77
10	64.038076	-24.069532	4.19	2.44e-18	7473.01	2.57	3.22e-18	7478.10	2.73	1.32
Spo-1	64.038565	-24.069939	1.90	4.30e-18	7472.55	3.13	5.49e-18	7478.01	2.89	1.28
Spo-2	64.038998	-24.070241	0.00	4.37e-18	7472.46	4.00	6.10e-18	7478.22	3.79	1.40

^aProperties of the O[II] lines were derived from 1-D spectra extracted from the MUSE data cube at 10 locations spaced 0''.6 apart along the length of the arc that comprises images 11.1 and 11.2 of the HFF14Spo host galaxy. Each extraction used an aperture of 0''.6 radius, centered on the mid-line of the host galaxy arc. The integrated line flux, observed wavelength of line center (λ_{center}), and full width at half maximum (FWHM) were found by fitting a Gaussian profile to each component of the doublet.

straint on the quiescent luminosity. Thus, instead of using a measured quiescent luminosity to estimate the build-up timescale, we assume that t_{rad} for HFF14Spo corresponds to the observed rest-frame lag between the two events, roughly 120 days (this accounts for both cosmic time dilation and a gravitational lensing time delay of ~ 40 days). Adopting $L_{\text{pk}} = 10^{41} \text{ erg s}^{-1}$ and $t_2 = 2$ days (see Figure 3), we infer that the quiescent luminosity of the HFF14Spo progenitor would be $L_{\text{qui}} \sim 10^{39.5} \text{ erg s}^{-1}$ ($M_V \sim -10$).

4.11. RN Light Curve Comparison

There are ten known RNe in the Milky Way galaxy, and seven of these exhibit outbursts that decline rapidly, fading by two magnitudes in less than ten days (Schaefer

2010). Figure 12 compares the HFF14Spo light curves to a composite light curve (the gray shaded region), which encompasses the V band light curve templates (Schaefer 2010) for all seven of these galactic RN events. The Andromeda galaxy (M31) also hosts at least one RN with a rapidly declining light curve. The 2014 eruption of this well-studied nova, M31N 2008a-12, is shown as a solid black line in Figure 12, fading by 2 mags in less than 3 days. This comparison demonstrates that the rapid decline of both of the HFF14Spo transient events is fully consistent with the eruptions of known RNe in the local universe.

4.12. RN Luminosity and Recurrence Period

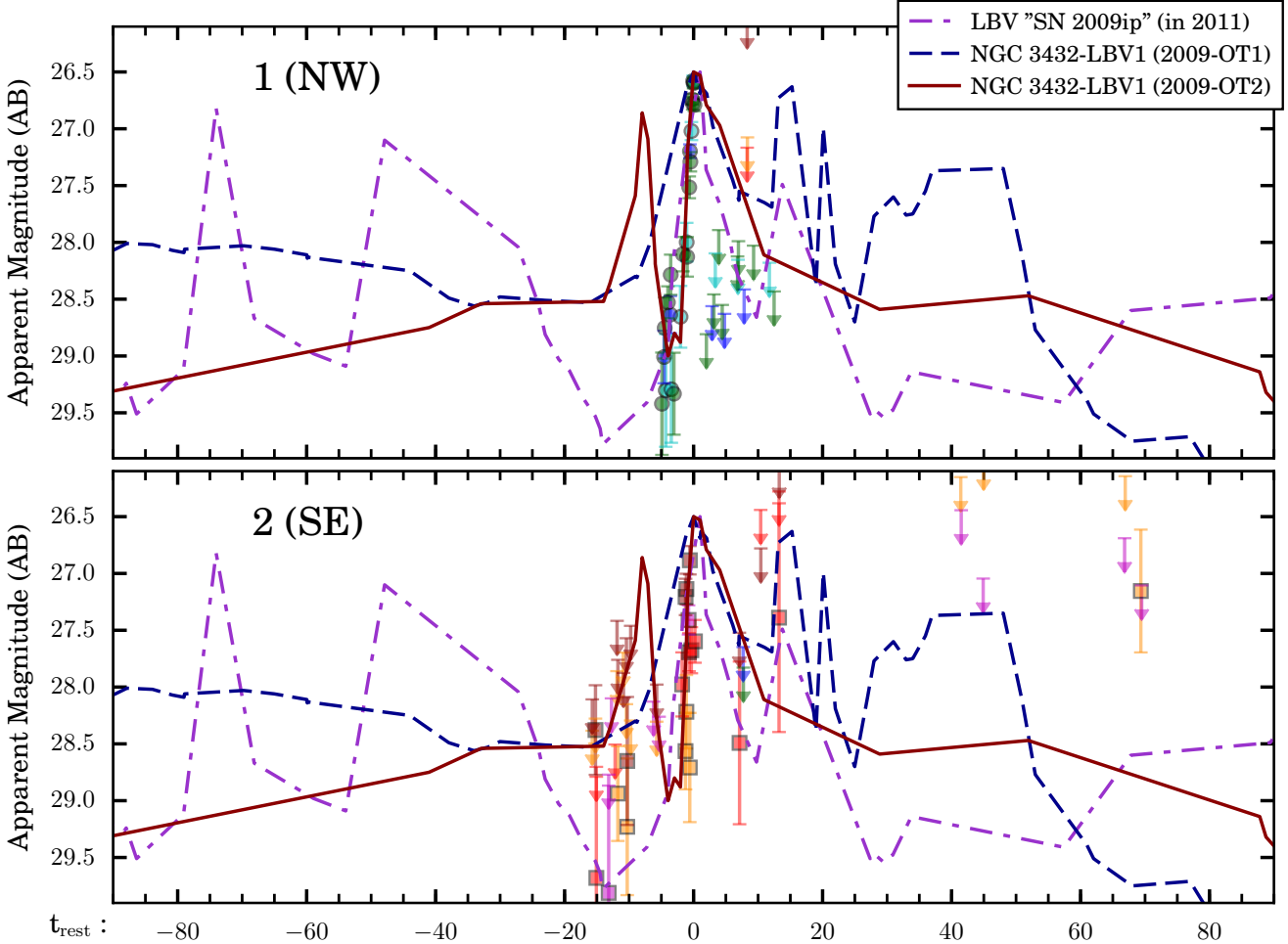


FIG. 11.— Comparison of observed HFF14Spo light curves against rapid outbursts from two LBVs. Colored markers show the HFF14Spo light curve data, as in Figure 2, with downward arrows marking 3σ upper limits in epochs with no detection of the HFF14Spo source. The LBV comparison light curves have been shifted in time and magnitude to match up with the peak of the observed light curves.

To examine the recurrence period and peak brightness of the HFF14Spo events relative to RNe, we rely on a pair of papers that evaluated an extensive grid of nova models through multiple cycles of outburst and quiescence (Prialnik and Kovetz 1995; Yaron *et al.* 2005). Figure 13 plots first the RN outburst amplitude (the apparent magnitude between outbursts minus the apparent magnitude at peak) and then the peak luminosity against the log of the recurrence period in years. For the HFF14Spo events we can only measure a lower limit on the outburst amplitude, since the presumed progenitor star is unresolved, so no measurement is available at quiescence. Figure 13 shows that a recurrence period as fast as one year is expected only for a RN system in which the primary WD is both very close to the Chandrasekhar mass limit ($1.4 M_{\odot}$) and also has an extraordinarily rapid mass transfer rate ($\sim 10^{-6} M_{\odot} \text{ yr}^{-1}$). The models of Yaron *et al.* (2005) suggest that such systems should have a very low peak amplitude (barely consistent with the lower limit for HFF14Spo) and a low peak luminosity (~ 100 times less luminous than the HFF14Spo events).

The closest analog for the HFF14Spo events from

the population of known RN systems is the nova M31N 2008a-12. Kato *et al.* (2015) provided a theoretical model that can account for the key observational characteristics of this remarkable nova: the very rapid recurrence timescale (< 1 yr), fast optical light curve ($t_2 \sim 2$ days), and short supersoft x-ray phase (6–18 days after optical outburst Henze *et al.* 2015b). To match these observations, Kato *et al.* invoke a $1.38 M_{\odot}$ white dwarf primary, drawing mass from a companion at a rate of $1.6 \times 10^{-7} M_{\odot} \text{ yr}^{-1}$. This is largely consistent with the theoretical expectations derived by Yaron *et al.* (2005), and reinforces the conclusion that a combination of a high mass white dwarf and efficient mass transfer are the key ingredients for rapid recurrence and short light curves. The one feature that cannot be effectively explained with this hypothesis is the peculiarly high luminosity of the HFF14Spo events – even after accounting for the very large uncertainties.

4.13. Intracluster Light

To estimate the mass of intracluster stars along the line of sight to the HFF14Spo events, we follow the pro-

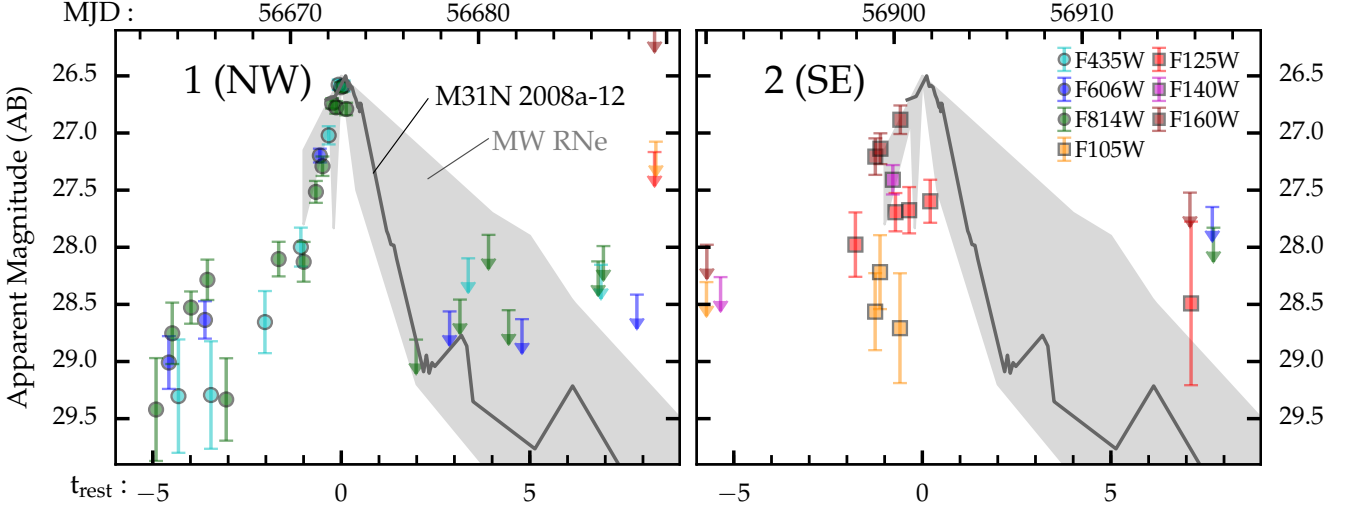


FIG. 12.— Comparison of the HFF14Spo light curves against template light curves for RN outbursts. Colored markers show the HFF14Spo light curve data, as in Figure 2, plotting the apparent magnitude as a function of time in the rest frame (bottom axis) and observer frame (top axis). The gray shaded regions encompass the outburst light curve shapes of 5 of the 11 known galactic RNe (U Sco, V2487 Oph, V394 CrA, T CrB, and V745 Sco), selected because they exhibit a rapid decline in their light curves (Schaefer 2010). The solid black line traces the 2014 outburst light curve shape for the rapid-recurrence nova M31N 2008a-12 (Darnley *et al.* 2014). All template light curves have been normalized to match the observed peaks of the HFF14Spo events.

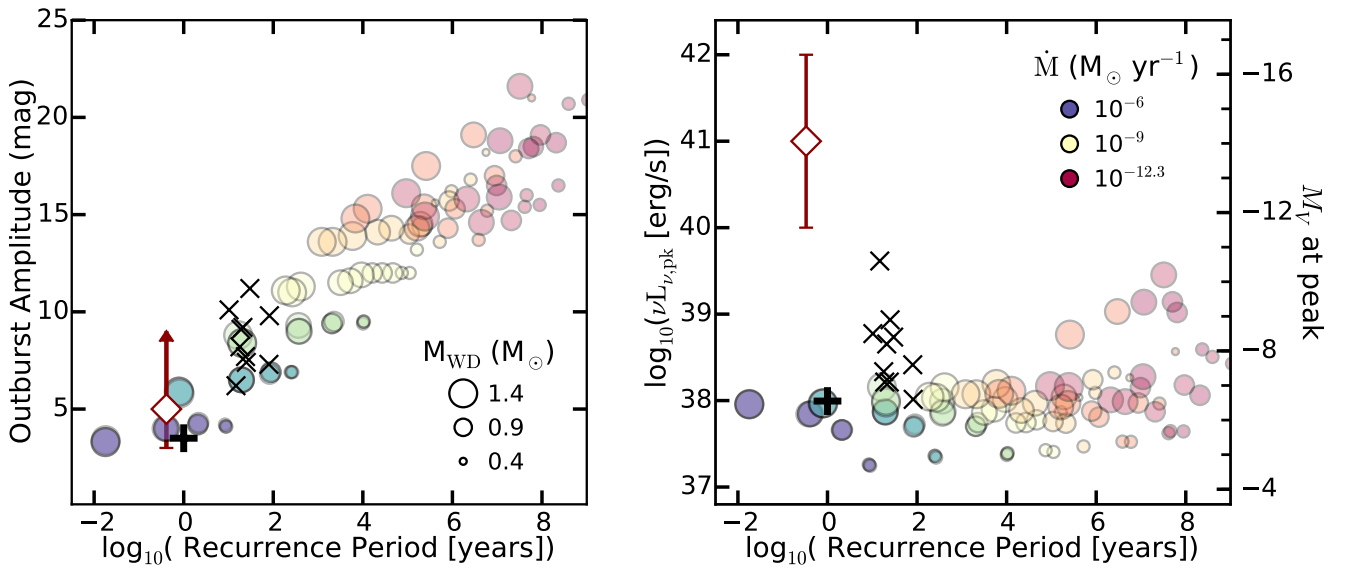


FIG. 13.— Comparison of the inferred HFF14Spo recurrence timescale against observed RNe and models. In the left panel the outburst amplitude in magnitudes is plotted against the recurrence timescale, while in the right panel the y axis shows the peak luminosity (or absolute magnitude). In both panels the joint constraints on HFF14Spo from both transient episodes are plotted as large open diamonds, observed constraints from the 10 galactic RNe appear as black ‘x’ points, and the rapid-recurrence nova M31N 2008a-12 is shown with a thick black ‘+’ marker. Colored circles show the results from a suite of numerical hydrodynamic simulations from Yaron *et al.* (2005). The size of each circle indicates the mass of the primary white dwarf (WD) star over the range $0.4\text{--}1.4 M_{\odot}$, as indicated in the legend of the left panel. The color of each circle denotes the rate of mass transfer from the secondary onto the WD, as given in the right panel’s legend.

cedure of Kelly et al. (in prep) and Morishita et al. (in prep). This entails fitting and removing the surface brightness of individual galaxies in the field, then fitting a smooth profile to the residual surface brightness of intracluster light (ICL). The surface brightness is then converted to a projected stellar mass surface density by assuming a Chabrier 2003 initial mass function and an exponentially declining star formation history. For further details, see Kelly et al. (in prep). This procedure leads to an estimate for the intracluster stellar mass of $\log(\Sigma_*/(M_\odot \text{ kpc}^{-2})) = 6.9 \pm 0.4$. This is very similar to the value of $6.8^{+0.4}_{-0.3}$ inferred for the probable caustic crossing star *Icarus* (Kelly et al., in prep).

4.14. Expected Timescale for Microlensing Events

A commonly observed example of microlensing-induced transient effects is when a bright background source (a quasar) by a galaxy-scale lens (Wambsganss 2001; Kochanek 2004). In this optically thick microlensing regime, the lensing potential along the line of sight to the quasar is composed of many stellar-mass objects. Each compact object along the line of sight generates a separate critical lensing curve, resulting in a complex web of overlapping critical curves. As all of these lensing stars are in motion relative to the background source, the web of caustics will shift across the source position, leading to a stochastic variability on timescales of months to years. This scenario is inconsistent with the observed data, as the two HFF14Spo events were far too short in duration and did not exhibit the repeated “flickering” variation that would be expected from optically thick microlensing.

For the cluster-scale lens relevant in the case of HFF14Spo, we should expect to be in the optically thin microlensing regime. This situation is similar to the “local” microlensing light curves observed when stars within our galaxy or neighboring dwarf galaxies pass behind a massive compact halo object (Paczynski 1986; Alcock *et al.* 1993; Aubourg *et al.* 1993; Udalski *et al.* 1993). In this case, an isolated microlensing event can occur if there is a background star (i.e., in the HFF14Spo host galaxy) that is the dominant source of luminosity in its environment. In practice this means that the source must be a very bright O or B star with mass of order $10 M_\odot$. Depending on its age, the size of such a star would range from a few to a few dozen times the size of the sun. The net relative transverse velocity would be on the order of a few 100 km s^{-1} , which is comparable to the orbital velocity of stars within a galaxy or galaxies within a cluster.

In the case of a smooth cluster potential, the timescale τ for the light curve of such a caustic crossing event is dictated by the radius of the source, R , and the net transverse velocity, v , of the source across the caustic (Chang and Refsdal 1979, 1984; MiraldaEscude 1991):

$$\tau = 6 \frac{R}{5 R_\odot} \frac{300 \text{ km s}^{-1}}{v} \text{ hr} \quad (3)$$

Thus, for reasonable assumptions about the star’s radius and velocity, the timescale τ is on the order of hours to days, which is well matched to the observed rise and decline timescales of the HFF14Spo events.

4.15. Color Curves

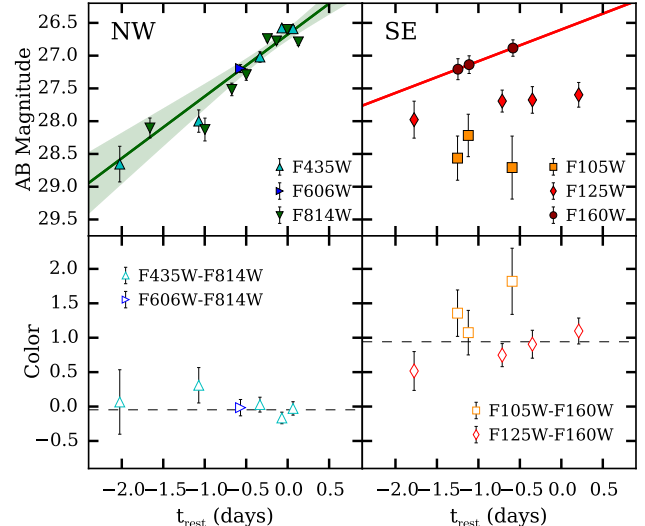


FIG. 14.— Observed colors for the HFF14Spo events. Filled points plotted in the top panels show observed AB magnitudes for the HFF14Spo-NW and HFF14Spo-SE events from -3 rest-frame days before the date of observed peak brightness. Solid lines and shaded regions show linear fits to the data in the F814W and F160W bands. Open points in the bottom panels show observed colors in the rest-frame bands. For each color the magnitude in the bluer band is the directly measured value, and the magnitude in the redder band is interpolated from the linear fits shown in the top panel. All colors are consistent with showing no evolution over the rising portion of each light curve.

At redshift $z = 1$ the observed optical and infrared bands translate to rest-frame ultraviolet (UV) and optical wavelengths, respectively. To derive rest-frame UV and optical colors from the observed photometry, we start with the measured magnitude in a relatively blue band (F435W and F606W for HFF14Spo-NW and F105W, F125W, F140W for HFF14Spo-SE). We then subtract the coeval magnitude for a matched red band (F814W for HFF14Spo-NW, F125W or F160W for HFF14Spo-SE), derived from the linear fits to those bands. To adjust these to rest-frame filters, we apply K corrections (following Hogg *et al.* 2002), which we compute by defining a crude SED via linear interpolation between the observed broad bands for each transient event at each epoch. For consistency with past published results, we include in each K correction a transformation from AB to Vega-based magnitudes. The resulting UV and optical colors are plotted in Figure 14. Both HFF14Spo-NW and HFF14Spo-SE show little or no color variation over the period where color information is available.

TABLE 4
PHOTOMETRY OF THE HFF14SPO-NW EVENT.

Date (MJD)	Filter	Flux ($10^{30} \text{ erg s}^{-1} \text{ cm}^{-2} \text{ Hz}^{-1}$)	AB Mag
56144.86	F105W	0.063 ± 0.119	<29.39
56184.90	F105W	-0.013 ± 0.178	<27.08
56689.43	F105W	-0.111 ± 0.179	<27.08
56869.98	F105W	-0.001 ± 0.075	<28.01
56870.98	F105W	0.068 ± 0.048	<29.32
56877.68	F105W	-0.084 ± 0.111	<27.59
56877.94	F105W	0.005 ± 0.051	<32.09
56879.67	F105W	0.008 ± 0.048	<31.71

TABLE 4 — *Continued*

Date (MJD)	Filter	Flux (10^{30} erg s $^{-1}$ cm $^{-2}$ Hz $^{-1}$)	AB Mag
56880.60	F105W	-0.003±0.057	<28.32
56880.86	F105W	-0.002±0.067	<28.14
56881.92	F105W	-0.065±0.100	<27.71
56890.02	F105W	-0.063±0.103	<27.68
56898.99	F105W	-0.005±0.079	<27.96
56899.25	F105W	0.001±0.083	<34.33
56900.31	F105W	0.014±0.067	<31.02
56984.58	F105W	-0.152±0.434	<26.11
56991.68	F105W	-0.242±0.396	<26.21
57035.72	F105W	0.172±0.202	<28.31
57040.57	F105W	0.460±0.211	27.24±0.50
56132.22	F110W	0.066±0.046	<29.35
56170.80	F110W	-0.179±0.251	<26.71
56159.62	F125W	-0.124±0.208	<26.91
56197.80	F125W	0.228±0.143	<28.00
56689.36	F125W	0.028±0.165	<30.27
56871.26	F125W	-0.037±0.069	<28.11
56877.09	F125W	0.010±0.048	<31.43
56897.94	F125W	-0.008±0.102	<27.69
56900.07	F125W	-0.063±0.116	<27.55
56900.80	F125W	0.089±0.060	<29.02
56901.92	F125W	0.061±0.056	<29.43
56915.79	F125W	0.024±0.125	<30.43
56922.36	F125W	0.393±0.360	<27.41
56928.07	F125W	0.095±0.166	<28.96
56159.63	F140W	-0.144±0.256	<26.69
56184.88	F140W	-0.103±0.186	<27.03
56875.10	F140W	-0.026±0.067	<28.14
56875.97	F140W	0.008±0.042	<31.70
56889.05	F140W	-0.019±0.081	<27.94
56890.77	F140W	-0.181±0.158	<27.21
56899.93	F140W	-0.126±0.148	<27.28
56984.72	F140W	-0.105±0.266	<26.65
56991.55	F140W	0.202±0.160	<28.14
57035.52	F140W	-0.272±0.393	<26.22
57040.83	F140W	0.004±0.239	<32.32
56132.24	F160W	-0.280±0.401	<26.20
56144.87	F160W	0.001±0.267	<34.03
56170.79	F160W	0.104±0.185	<28.85
56197.79	F160W	-0.239±0.332	<26.40
56689.36	F160W	-0.400±0.485	<25.99
56870.00	F160W	0.083±0.067	<29.10
56870.99	F160W	0.257±0.108	27.88±0.46
56877.70	F160W	-0.048±0.128	<27.44
56877.96	F160W	-0.008±0.101	<27.70
56879.69	F160W	-0.009±0.080	<27.95
56880.61	F160W	0.035±0.069	<30.05
56880.88	F160W	-0.185±0.239	<26.76
56881.94	F160W	-0.070±0.141	<27.34
56890.04	F160W	-0.111±0.152	<27.26
56899.00	F160W	-0.064±0.141	<27.33
56899.27	F160W	-0.147±0.176	<27.09
56900.33	F160W	-0.014±0.122	<27.50
56915.73	F160W	-0.021±0.208	<26.91
56922.41	F160W	-0.120±0.313	<26.47
56928.13	F160W	-0.186±0.352	<26.34
56159.54	F435W	0.012±0.016	<31.23
56184.77	F435W	-0.001±0.010	<30.23
56664.04	F435W	0.069±0.031	29.30±0.50
56665.77	F435W	0.070±0.030	29.29±0.47
56668.64	F435W	0.125±0.031	28.66±0.27
56670.55	F435W	0.229±0.036	28.00±0.17
56672.03	F435W	0.565±0.041	27.02±0.08
56672.56	F435W	0.849±0.035	26.58±0.05
56672.83	F435W	0.840±0.038	26.59±0.05
56679.45	F435W	-0.065±0.070	<28.10
56686.51	F435W	-0.056±0.066	<28.15
56696.27	F435W	-0.030±0.065	<28.18
56144.78	F606W	-0.021±0.017	<30.59
56170.73	F606W	-0.117±0.110	<29.89
56663.53	F606W	0.090±0.019	29.01±0.23
56665.45	F606W	0.127±0.019	28.64±0.16
56671.56	F606W	0.480±0.027	27.20±0.06
56678.46	F606W	-0.059±0.046	<28.56
56682.31	F606W	-0.060±0.043	<28.63
56688.42	F606W	-0.067±0.052	<28.41

TABLE 4 — *Continued*

Date (MJD)	Filter	Flux (10^{30} erg s $^{-1}$ cm $^{-2}$ Hz $^{-1}$)	AB Mag
56916.92	F606W	-0.020±0.064	<28.20
56144.80	F814W	0.314±0.317	<27.66
56157.83	F814W	0.028±0.041	<30.29
56170.72	F814W	-0.108±0.109	<27.61
56184.75	F814W	0.004±0.007	<32.47
56662.85	F814W	0.062±0.026	29.42±0.45
56663.71	F814W	0.114±0.028	28.75±0.27
56664.71	F814W	0.141±0.018	28.53±0.14
56665.58	F814W	0.176±0.029	28.28±0.18
56666.58	F814W	0.067±0.022	29.33±0.36
56669.37	F814W	0.208±0.029	28.10±0.15
56670.70	F814W	0.204±0.033	28.13±0.17
56671.35	F814W	0.358±0.032	27.52±0.10
56671.70	F814W	0.440±0.034	27.29±0.09
56672.21	F814W	0.731±0.031	26.74±0.05
56672.43	F814W	0.707±0.036	26.78±0.06
56672.69	F814W	0.832±0.035	26.60±0.05
56672.96	F814W	0.698±0.035	26.79±0.06
56676.68	F814W	0.019±0.036	<30.68
56679.01	F814W	-0.015±0.050	<28.46
56680.53	F814W	-0.109±0.084	<27.89
56681.60	F814W	-0.021±0.046	<28.55
56686.36	F814W	-0.053±0.068	<28.12
56686.64	F814W	-0.092±0.077	<27.99
56691.36	F814W	-0.074±0.074	<28.03
56697.73	F814W	-0.040±0.051	<28.43
56916.98	F814W	0.007±0.093	<31.86

TABLE 5
PHOTOMETRY OF THE HFF14SPO-SE EVENT.

Date (MJD)	Filter	Flux (10^{30} erg s $^{-1}$ cm $^{-2}$ Hz $^{-1}$)	AB Mag
56144.86	F105W	-0.127±0.206	<26.92
56184.90	F105W	0.120±0.169	<28.70
56689.43	F105W	-0.100±0.170	<27.13
56869.98	F105W	0.041±0.054	<29.88
56870.98	F105W	0.009±0.059	<31.56
56877.68	F105W	-0.031±0.087	<27.86
56877.94	F105W	0.097±0.037	28.94±0.42
56879.67	F105W	-0.078±0.101	<27.70
56880.60	F105W	-0.022±0.066	<28.15
56880.86	F105W	0.074±0.041	<29.23
56881.92	F105W	0.034±0.058	<30.06
56890.02	F105W	0.046±0.058	<29.73
56898.99	F105W	0.136±0.042	28.56±0.34
56899.25	F105W	0.187±0.056	28.22±0.32
56900.31	F105W	0.119±0.053	28.71±0.48
56984.58	F105W	-0.151±0.419	<26.15
56991.68	F105W	-0.404±0.498	<25.96
57035.72	F105W	-0.265±0.422	<26.14
57040.57	F105W	0.499±0.248	27.15±0.54
56132.22	F110W	0.050±0.045	<29.64
56170.80	F110W	-0.230±0.307	<26.49
56159.62	F125W	-0.329±0.387	<26.24
56197.80	F125W	-0.226±0.310	<26.48
56689.36	F125W	-0.076±0.190	<27.01
56871.26	F125W	0.049±0.040	<29.68
56877.09	F125W	0.009±0.048	<31.51
56897.94	F125W	0.234±0.061	27.98±0.28
56900.07	F125W	0.304±0.047	27.69±0.17
56900.80	F125W	0.309±0.058	27.68±0.20
56901.92	F125W	0.332±0.058	27.60±0.19
56915.79	F125W	0.146±0.096	<28.49
56922.36	F125W	-0.275±0.321	<26.44
56928.07	F125W	0.402±0.373	<27.39
56159.63	F140W	-0.006±0.159	<27.21
56184.88	F140W	-0.077±0.168	<27.14
56875.10	F140W	0.043±0.038	<29.81
56875.97	F140W	-0.045±0.070	<28.10
56889.05	F140W	0.042±0.068	<29.85

TABLE 5 — *Continued*

Date (MJD)	Filter	Flux (10^{30} erg s $^{-1}$ cm $^{-2}$ Hz $^{-1}$)	AB Mag
56890.77	F140W	0.055±0.060	<29.55
56899.93	F140W	0.395±0.047	27.41±0.13
56984.72	F140W	-0.226±0.320	<26.44
56991.55	F140W	0.003±0.184	<32.56
57035.52	F140W	-0.068±0.255	<26.69
57040.83	F140W	0.142±0.174	<28.52
56132.24	F160W	-0.196±0.355	<26.33
56144.87	F160W	-0.592±0.716	<25.57
56170.79	F160W	-0.375±0.461	<26.05
56197.79	F160W	-0.766±0.725	<25.56
56689.36	F160W	-0.282±0.405	<26.19
56870.00	F160W	0.028±0.069	<30.30
56870.99	F160W	0.162±0.059	28.38±0.39
56877.70	F160W	-0.047±0.131	<27.42
56877.96	F160W	-0.002±0.095	<27.76
56879.69	F160W	0.004±0.086	<32.34
56880.61	F160W	-0.043±0.113	<27.57
56880.88	F160W	0.126±0.065	<28.65
56881.94	F160W	-0.026±0.125	<27.46
56890.04	F160W	0.035±0.078	<30.05
56899.00	F160W	0.476±0.070	27.21±0.16
56899.27	F160W	0.507±0.063	27.14±0.13
56900.33	F160W	0.640±0.074	26.88±0.12
56915.73	F160W	0.053±0.119	<29.59
56922.41	F160W	0.037±0.235	<29.99
56928.13	F160W	-0.281±0.466	<26.04
56159.54	F435W	0.002±0.007	<33.06
56184.77	F435W	-0.009±0.013	<29.93
56664.04	F435W	0.033±0.034	<30.11
56665.77	F435W	-0.019±0.039	<28.73
56668.64	F435W	0.044±0.035	<29.79
56670.55	F435W	0.047±0.043	<29.71
56672.03	F435W	0.051±0.039	<29.63
56672.56	F435W	-0.046±0.065	<28.18
56672.83	F435W	-0.064±0.075	<28.01
56679.45	F435W	0.018±0.035	<30.74
56686.51	F435W	-0.026±0.052	<28.41
56696.27	F435W	0.009±0.049	<31.48
56144.78	F606W	0.234±0.176	<27.98
56170.73	F606W	0.043±0.061	<29.81
56663.53	F606W	0.004±0.027	<32.27
56665.45	F606W	0.016±0.026	<30.91
56671.56	F606W	-0.021±0.043	<28.61
56678.46	F606W	-0.012±0.029	<29.05
56682.31	F606W	-0.016±0.035	<28.83
56688.42	F606W	0.033±0.024	<30.10
56916.92	F606W	-0.121±0.106	<27.65
56144.80	F814W	-0.294±0.274	<26.61
56157.83	F814W	-0.025±0.146	<27.29
56170.72	F814W	-0.027±0.127	<27.45
56184.75	F814W	0.037±0.010	29.97±0.29
56662.85	F814W	0.026±0.036	<30.37
56663.71	F814W	-0.019±0.052	<28.42
56664.71	F814W	0.005±0.026	<32.15
56665.58	F814W	-0.056±0.072	<28.07
56666.58	F814W	-0.007±0.038	<28.75
56669.37	F814W	0.010±0.042	<31.44
56670.70	F814W	0.005±0.042	<32.12
56671.35	F814W	0.075±0.029	29.21±0.41
56671.70	F814W	0.209±0.156	<28.10
56672.21	F814W	-0.014±0.054	<28.38
56672.43	F814W	0.005±0.041	<32.14
56672.69	F814W	-0.003±0.036	<28.81
56672.96	F814W	-0.020±0.053	<28.41
56676.68	F814W	-0.005±0.042	<28.64
56679.01	F814W	0.016±0.040	<30.89
56680.53	F814W	-0.009±0.045	<28.57
56681.60	F814W	0.012±0.037	<31.22
56686.36	F814W	-0.031±0.055	<28.35
56686.64	F814W	-0.031±0.050	<28.45
56691.36	F814W	0.042±0.036	<29.84
56697.73	F814W	0.064±0.019	29.39±0.31
56916.98	F814W	-0.028±0.089	<27.83

TABLE 5 — *Continued*

Date (MJD)	Filter	Flux (10^{30} erg s $^{-1}$ cm $^{-2}$ Hz $^{-1}$)	AB Mag
---------------	--------	---	--------

REFERENCES

- S. A. Rodney, B. Patel, D. Scolnic, R. J. Foley, A. Molino, G. Brammer, M. Jauzac, M. Bradač, T. Broadhurst, D. Coe, J. M. Diego, O. Graur, J. Hjorth, A. Hoag, S. W. Jha, T. L. Johnson, P. Kelly, D. Lam, C. McCully, E. Medezinski, M. Meneghetti, J. Merten, J. Richard, A. Riess, K. Sharon, L.-G. Strolger, T. Treu, X. Wang, L. L. R. Williams, and A. Zitrin, *ApJ* **811**, 70 (2015).
- P. L. Kelly, S. A. Rodney, T. Treu, R. J. Foley, G. Brammer, K. B. Schmidt, A. Zitrin, A. Sonnenfeld, L.-G. Strolger, O. Graur, A. V. Filippenko, S. W. Jha, A. G. Riess, M. Bradac, B. J. Weiner, D. Scolnic, M. A. Malkan, A. von der Linden, M. Trenti, J. Hjorth, R. Gavazzi, A. Fontana, J. C. Merten, C. McCully, T. Jones, M. Postman, A. Dressler, B. Patel, S. B. Cenko, M. L. Graham, and B. E. Tucker, *Science* **347**, 1123 (2015).
- P. L. Kelly, J. M. Diego, S. A. Rodney, N. Kaiser, and et al., submitted (2017).
- A. Pastorello, E. Cappellaro, C. Inserra, S. J. Smartt, G. Pignata, S. Benetti, S. Valenti, M. Fraser, K. Takáts, S. Benitez, M. T. Botticella, J. Brimacombe, F. Bufano, F. Cellier-Holzem, M. T. Costado, G. Cupani, I. Curtis, N. Elias-Rosa, M. Ergon, J. P. U. Fynbo, F.-J. Hambisch, M. Hamuy, A. Harutyunyan, K. M. Ivarson, E. Kankare, J. C. Martin, R. Kotak, A. P. LaCluyze, K. Maguire, S. Mattila, J. Maza, M. McCrum, M. Miluzio, H. U. Norgaard-Nielsen, M. C. Nysewander, P. Ochner, Y.-C. Pan, M. L. Pumo, D. E. Reichart, T. G. Tan, S. Taubenberger, L. Tomasella, M. Turatto, and D. Wright, *ApJ* **767**, 1 (2013).
- A. Pastorello, M. T. Botticella, C. Trundle, S. Taubenberger, S. Mattila, E. Kankare, N. Elias-Rosa, S. Benetti, G. Duszanowicz, L. Hermansson, J. E. Beckman, F. Bufano, M. Fraser, A. Harutyunyan, H. Navasardyan, S. J. Smartt, S. D. van Dyk, J. S. Vink, and R. M. Wagner, *MNRAS* **408**, 181 (2010).
- A. Zitrin, M. Meneghetti, K. Umetsu, T. Broadhurst, M. Bartelmann, R. Bouwens, L. Bradley, M. Carrasco, D. Coe, H. Ford, D. Kelson, A. M. Koekemoer, E. Medezinski, J. Moustakas, L. A. Moustakas, M. Nonino, M. Postman, P. Rosati, G. Seidel, S. Seitz, I. Sendra, X. Shu, J. Vega, and W. Zheng, *ApJ* **762**, L30 (2013).
- M. Jauzac, B. Clément, M. Limousin, J. Richard, E. Jullo, H. Ebeling, H. Atek, J.-P. Kneib, K. Knowles, P. Natarajan, D. Eckert, E. Egami, R. Massey, and M. Rexroth, *MNRAS* **443**, 1549 (2014).
- T. L. Johnson, K. Sharon, M. B. Bayliss, M. D. Gladders, D. Coe, and H. Ebeling, *ApJ* **797**, 48 (2014).
- J. Richard, M. Jauzac, M. Limousin, E. Jullo, B. Clément, H. Ebeling, J.-P. Kneib, H. Atek, P. Natarajan, E. Egami, R. Livermore, and R. Bower, *MNRAS* **444**, 268 (2014).
- J. M. Diego, T. Broadhurst, N. Benitez, K. Umetsu, D. Coe, I. Sendra, M. Sereno, L. Izzo, and G. Covone, *MNRAS* **446**, 683 (2015).
- C. Grillo, S. H. Suyu, P. Rosati, A. Mercurio, I. Balestra, E. Munari, M. Nonino, G. B. Caminha, M. Lombardi, G. De Lucia, S. Borgani, R. Gobat, A. Biviano, M. Girardi, K. Umetsu, D. Coe, A. M. Koekemoer, M. Postman, A. Zitrin, A. Halkola, T. Broadhurst, B. Sartoris, V. Presotto, M. Annunziatella, C. Maier, A. Fritz, E. Vanzella, and B. Frye, *ApJ* **800**, 38 (2015).
- A. Hoag, K.-H. Huang, T. Treu, M. Bradač, K. B. Schmidt, X. Wang, G. B. Brammer, A. Broussard, R. Amorin, M. Castellano, A. Fontana, E. Merlin, T. Schrabback, M. Trenti, and B. Vulcani, *ApJ* **831**, 182 (2016).
- K. Sebesta, L. L. R. Williams, I. Mohammed, P. Saha, and J. Liesenborgs, *MNRAS* **461**, 2126 (2016).
- G. B. Caminha, C. Grillo, P. Rosati, I. Balestra, A. Mercurio, E. Vanzella, A. Biviano, K. I. Caputi, C. Delgado-Correal, W. Karman, M. Lombardi, M. Meneghetti, B. Sartoris, and P. Tozzi, *A&A* **600**, A90 (2017).
- L. A. Balona, *MNRAS* **423**, 3420 (2012).

- C. Karoff, M. F. Knudsen, P. De Cat, A. Bonanno, A. Fogtmann-Schulz, J. Fu, A. Frasca, F. Inceoglu, J. Olsen, Y. Zhang, Y. Hou, Y. Wang, J. Shi, and W. Zhang, *Nature Communications* **7**, 11058 (2016).
- C. M. Gaskell and E. S. Klimek, *Astronomical and Astrophysical Transactions* **22**, 661 (2003).
- S. R. Kulkarni, E. O. Ofek, A. Rau, S. B. Cenko, A. M. Soderberg, D. B. Fox, A. Gal-Yam, P. L. Capak, D. S. Moon, W. Li, A. V. Filippenko, E. Egami, J. Kartaltepe, and D. B. Sanders, *Nature* **447**, 458 (2007).
- A. Gal-Yam, *Science* **337**, 927 (2012).
- I. Arcavi, W. M. Wolf, D. A. Howell, L. Bildsten, G. Leloudas, D. Hardin, S. Prajs, D. A. Perley, G. Svirski, A. Gal-Yam, B. Katz, C. McCully, S. B. Cenko, C. Lidman, M. Sullivan, S. Valenti, P. Astier, C. Balland, R. G. Carlberg, A. Conley, D. Fouchez, J. Guy, R. Pain, N. Palanque-Delabrouille, K. Perrett, C. J. Pritchett, N. Regnault, J. Rich, and V. Ruhlmann-Kleider, *ApJ* **819**, 35 (2016).
- W. Li, A. V. Filippenko, R. Chornock, E. Berger, P. Berlind, M. L. Calkins, P. Challis, C. Fassnacht, S. Jha, R. P. Kirshner, T. Matheson, W. L. W. Sargent, R. A. Simcoe, G. H. Smith, and G. Squires, *PASP* **115**, 453 (2003).
- S. Jha, D. Branch, R. Chornock, R. J. Foley, W. Li, B. J. Swift, D. Casebeer, and A. V. Filippenko, *AJ* **132**, 189 (2006).
- R. J. Foley, P. J. Challis, R. Chornock, M. Ganeshalingam, W. Li, G. H. Marion, N. I. Morrell, G. Pignata, M. D. Stritzinger, J. M. Silverman, X. Wang, J. P. Anderson, A. V. Filippenko, W. L. Freedman, M. Hamuy, S. W. Jha, R. P. Kirshner, C. McCully, S. E. Persson, M. M. Phillips, D. E. Reichtart, and A. M. Soderberg, *ApJ* **767**, 57 (2013).
- M. R. Drout, R. Chornock, A. M. Soderberg, N. E. Sanders, R. McKinnon, A. Rest, R. J. Foley, D. Milisavljevic, R. Margutti, E. Berger, M. Calkins, W. Fong, S. Gezari, M. E. Huber, E. Kankare, R. P. Kirshner, C. Leibler, R. Lunnan, S. Mattila, G. H. Marion, G. Narayan, A. G. Riess, K. C. Roth, D. Scolnic, S. J. Smartt, J. L. Tonry, W. S. Burgett, K. C. Chambers, K. W. Hodapp, R. Jedicek, N. Kaiser, E. A. Magnier, N. Metcalfe, J. S. Morgan, P. A. Price, and C. Waters, *ApJ* **794**, 23 (2014).
- A. V. Filippenko, R. Chornock, B. Swift, M. Modjaz, R. Simcoe, and M. Rauch, *IAU Circ.* **8159** (2003).
- H. B. Perets, C. Badenes, I. Arcavi, J. D. Simon, and A. Gal-yam, *ApJ* **730**, 89 (2011).
- M. M. Kasliwal, S. R. Kulkarni, A. Gal-Yam, P. E. Nugent, M. Sullivan, L. Bildsten, O. Yaron, H. B. Perets, I. Arcavi, S. Ben-Ami, V. B. Bhalerao, J. S. Bloom, S. B. Cenko, A. V. Filippenko, D. A. Frail, M. Ganeshalingam, A. Horesh, D. A. Howell, N. M. Law, D. C. Leonard, W. Li, E. O. Ofek, D. Polishook, D. Poznanski, R. M. Quimby, J. M. Silverman, A. Sternberg, and D. Xu, *ApJ* **755**, 161 (2012).
- U. Munari, A. Henden, S. Kiyota, D. Laney, F. Marang, T. Zwitter, R. L. M. Corradi, S. Desidera, P. M. Marrese, E. Giro, F. Boschi, and M. B. Schwartz, *A&A* **389**, L51 (2002).
- M. M. Kasliwal, S. R. Kulkarni, I. Arcavi, R. M. Quimby, E. O. Ofek, P. Nugent, J. Jacobsen, A. Gal-Yam, Y. Green, O. Yaron, D. B. Fox, J. L. Howell, S. B. Cenko, I. Kleiser, J. S. Bloom, A. Miller, W. Li, A. V. Filippenko, D. Starr, D. Poznanski, N. M. Law, G. Helou, D. A. Frail, J. D. Neill, K. Forster, D. C. Martin, S. P. Tendulkar, N. Gehrels, J. Kennea, M. Sullivan, L. Bildsten, R. Dekany, G. Rahmer, D. Hale, R. Smith, J. Zolkower, V. Velur, R. Walters, J. Henning, K. Bui, D. McKenna, and C. Blake, *ApJ* **730**, 134 (2011a).
- L.-X. Li and B. Paczyński, *ApJ* **507**, L59 (1998).
- S. R. Kulkarni, *ArXiv Astrophysics e-prints* (2005).
- B. Warner, *Ap&SS* **225**, 249 (1995).
- G. Nelemans and C. A. Tout, *MNRAS* **356**, 753 (2005).
- L. Bildsten, K. J. Shen, N. N. Weinberg, and G. Nelemans, *ApJ* **662**, L95 (2007).
- B. D. Metzger, G. Martínez-Pinedo, S. Darbha, E. Quataert, A. Arcones, D. Kasen, R. Thomas, P. Nugent, I. V. Panov, and N. T. Zinner, *MNRAS* **406**, 2650 (2010).
- J. Barnes and D. Kasen, *ApJ* **775**, 18 (2013).
- D. Kasen, R. Fernández, and B. D. Metzger, *MNRAS* **450**, 1777 (2015).
- K. J. Shen, D. Kasen, N. N. Weinberg, L. Bildsten, and E. Scannapieco, *ApJ* **715**, 767 (2010).
- D. A. Perley, B. D. Metzger, J. Granot, N. R. Butler, T. Sakamoto, E. Ramirez-Ruiz, A. J. Levan, J. S. Bloom, A. A. Miller, A. Bunker, H.-W. Chen, A. V. Filippenko, N. Gehrels, K. Glazebrook, P. B. Hall, K. C. Hurley, D. Kocevski, W. Li, S. Lopez, J. Norris, A. L. Piro, D. Poznanski, J. X. Prochaska, E. Quataert, and N. Tanvir, *ApJ* **696**, 1871 (2009).
- N. R. Tanvir, A. J. Levan, A. S. Fruchter, J. Hjorth, R. A. Hounsell, K. Wiersema, and R. L. Tunnicliffe, *Nature* **500**, 547 (2013).
- M. M. Kasliwal, S. R. Kulkarni, A. Gal-Yam, O. Yaron, R. M. Quimby, E. O. Ofek, P. Nugent, D. Poznanski, J. Jacobsen, A. Sternberg, I. Arcavi, D. A. Howell, M. Sullivan, D. J. Rich, P. F. Burke, J. Brimacombe, D. Milisavljevic, R. Fesen, L. Bildsten, K. Shen, S. B. Cenko, J. S. Bloom, E. Hsiao, N. M. Law, N. Gehrels, S. Immler, R. Dekany, G. Rahmer, D. Hale, R. Smith, J. Zolkower, V. Velur, R. Walters, J. Henning, K. Bui, and D. McKenna, *ApJ* **723**, L98 (2010).
- H. B. Perets, A. Gal-Yam, P. A. Mazzali, D. Arnett, D. Kagan, A. V. Filippenko, W. Li, I. Arcavi, S. B. Cenko, D. B. Fox, D. C. Leonard, D.-S. Moon, D. J. Sand, A. M. Soderberg, J. P. Anderson, P. Å. James, R. J. Foley, M. Ganeshalingam, E. O. Ofek, L. Bildsten, G. Nelemans, K. J. Shen, N. N. Weinberg, B. D. Metzger, A. L. Piro, E. Quataert, M. Kiewe, and D. Poznanski, *Nature* **465**, 322 (2010).
- D. Poznanski, R. Chornock, P. E. Nugent, J. S. Bloom, A. V. Filippenko, M. Ganeshalingam, D. C. Leonard, W. Li, and R. C. Thomas, *Science* **327**, 58 (2010).
- P. L. Kelly, S. A. Rodney, T. Treu, L.-G. Strolger, R. J. Foley, S. W. Jha, J. Selsing, G. Brammer, M. Bradač, S. B. Cenko, O. Graur, A. V. Filippenko, J. Hjorth, C. McCully, A. Molino, M. Nonino, A. G. Riess, K. B. Schmidt, B. Tucker, A. von der Linden, B. J. Weiner, and A. Zitrin, *ApJ* **819**, L8 (2016).
- D. Poznanski, N. Butler, A. V. Filippenko, M. Ganeshalingam, W. Li, J. S. Bloom, R. Chornock, R. J. Foley, P. E. Nugent, J. M. Silverman, S. B. Cenko, E. L. Gates, D. C. Leonard, A. A. Miller, M. Modjaz, F. J. D. Serduke, N. Smith, B. J. Swift, and D. S. Wong, *ApJ* **694**, 1067 (2009).
- E. Berger, C. N. Leibler, R. Chornock, A. Rest, R. J. Foley, A. M. Soderberg, P. A. Price, W. S. Burgett, K. C. Chambers, H. Flewelling, M. E. Huber, E. A. Magnier, N. Metcalfe, C. W. Stubbs, and J. L. Tonry, *ApJ* **779**, 18 (2013).
- N. Smith, W. Li, J. M. Silverman, M. Ganeshalingam, and A. V. Filippenko, *MNRAS* **415**, 773 (2011).
- C. S. Kochanek, D. M. Szczygiel, and K. Z. Stanek, *ApJ* **758**, 142 (2012).
- J. Maza, M. Hamuy, R. Antezana, L. Gonzalez, P. Gonzalez, S. Lopez, G. Silva, et al., *CBET* 1 (2009).
- A. A. Miller, W. Li, P. E. Nugent, J. S. Bloom, A. V. Filippenko, and A. T. Merritt, *The Astronomer's Telegram* **2183** (2009).
- W. Li, N. Smith, A. A. Miller, and A. V. Filippenko, *The Astronomer's Telegram* **2212** (2009).
- E. Berger, R. Foley, and I. Ivans, *The Astronomer's Telegram* **2184** (2009).
- A. J. Drake, J. L. Prieto, S. G. Djorgovski, A. A. Mahabal, M. J. Graham, R. Williams, R. H. McNaught, M. Catelan, E. Christensen, E. C. Beshore, S. M. Larson, and S. Howerton, *The Astronomer's Telegram* **2897** (2010).
- N. Smith and S. P. Owocki, *ApJ* **645**, L45 (2006).
- S. E. Woosley, D. Kasen, S. Blinnikov, and E. Sorokina, *ApJ* **662**, 487 (2007).
- L. Dessart, E. Livne, and R. Waldman, *MNRAS* **405**, 2113 (2010).
- M. Della Valle and M. Livio, *ApJ* **452**, 704 (1995).
- R. A. Downes and H. W. Duerbeck, *AJ* **120**, 2007 (2000).
- A. W. Shafter, M. J. Darnley, K. Hornoch, A. V. Filippenko, M. F. Bode, R. Ciardullo, K. A. Misselt, R. A. Hounsell, R. Chornock, and T. Matheson, *ApJ* **734**, 12 (2011).
- M. M. Kasliwal, S. B. Cenko, S. R. Kulkarni, E. O. Ofek, R. Quimby, and A. Rau, *ApJ* **735**, 94 (2011b).
- B. E. Schaefer, *ApJS* **187**, 275 (2010).
- S. Tang, L. Bildsten, W. M. Wolf, K. L. Li, A. K. H. Kong, Y. Cao, S. B. Cenko, A. De Cia, M. M. Kasliwal, S. R. Kulkarni, R. R. Laher, F. Masci, P. E. Nugent, D. A. Perley, T. A. Prince, and J. Surace, *ApJ* **786**, 61 (2014).
- M. J. Darnley, S. C. Williams, M. F. Bode, M. Henize, J.-U. Ness, A. W. Shafter, K. Hornoch, and V. Votruba, *A&A* **563**, L9 (2014).
- M. J. Darnley, M. Henze, I. A. Steele, M. F. Bode, V. A. R. M. Ribeiro, P. Rodríguez-Gil, A. W. Shafter, S. C. Williams, D. Baer, I. Hachisu, M. Hernanz, K. Hornoch, R. Hounsell, M. Kato, S. Kiyota, H. Kućáková, H. Maehara, J.-U. Ness, A. S. Piascik, G. Sala, I. Skillen, R. J. Smith, and M. Wolf, *A&A* **580**, A45 (2015).
- M. Henze, M. J. Darnley, F. Kabashima, K. Nishiyama, K. Itagaki, and X. Gao, *A&A* **582**, L8 (2015a).
- M. Henze, J.-U. Ness, M. J. Darnley, M. F. Bode, S. C. Williams, A. W. Shafter, G. Sala, M. Kato, I. Hachisu, and M. Hernanz, *A&A* **580**, A46 (2015b).
- I. Hachisu and M. Kato, *ApJS* **167**, 59 (2006).
- P. Schneider and A. Weiss, *A&A* **164**, 237 (1986).
- J. MiraldaEscude, *ApJ* **379**, 94 (1991).
- G. F. Lewis, J. Miralda-Escude, D. C. Richardson, and J. Wambsganss, *MNRAS* **261**, 647 (1993).

- D. O. Jones, D. M. Scolnic, and S. A. Rodney, "PythonPhot: Simple DAOPHOT-type photometry in Python," *Astrophysics Source Code Library* (2015).
- J. Vernet, H. Dekker, S. D'Odorico, L. Kaper, P. Kjaergaard, F. Hammer, S. Randich, F. Zerbi, P. J. Groot, J. Hjorth, I. Guinouard, R. Navarro, T. Adolfse, P. W. Albers, J.-P. Amans, J. J. Andersen, M. I. Andersen, P. Binetruy, P. Bristol, R. Castillo, F. Chemla, L. Christensen, P. Conconi, R. Conzelmann, J. Dam, V. de Caprio, A. de Ugarte Postigo, B. Delabre, P. di Marcantonio, M. Downing, E. Elswijk, G. Finger, G. Fischer, H. Flores, P. François, P. Goldoni, L. Guglielmi, R. Haigron, H. Hanenburg, I. Hendriks, M. Horrobin, D. Horville, N. C. Jessen, F. Kerber, L. Kern, M. Kiekebusch, P. Kleszcz, J. Klougart, J. Kragt, H. H. Larsen, J.-L. Lizon, C. Lucuix, V. Mainieri, R. Manuputy, C. Martayan, E. Mason, R. Mazzoleni, N. Michaelsen, A. Modigliani, S. Moehler, P. Möller, A. Norup Sørensen, P. Nørregaard, C. Péroux, F. Patat, E. Pena, J. Pragt, C. Reiner, F. Rigal, M. Riva, R. Roelfsema, F. Royer, G. Sacco, P. Santin, T. Schoenmaker, P. Spano, E. Sweers, R. Ter Horst, M. Tintori, N. Tromp, P. van Dael, H. van der Vliet, L. Venema, M. Vidali, J. Vinther, P. Vola, R. Winters, D. Wistisen, G. Wulterkens, and A. Zacchei, *A&A* **536**, A105 (2011).
- N. Benítez, *ApJ* **536**, 571 (2000).
- G. B. Brammer, P. G. van Dokkum, and P. Coppi, *ApJ* **686**, 1503 (2008).
- O. Le Fèvre, M. Saisse, D. Mancini, S. Brau-Nogue, O. Caputi, L. Castinel, S. D'Odorico, B. Garilli, M. Kissler-Patig, C. Lucuix, G. Mancini, A. Pauget, G. Sciarretta, M. Scodéggi, L. Tresse, and G. Vettolani, in *Instrument Design and Performance for Optical/Infrared Ground-based Telescopes*, Society of Photo-Optical Instrumentation Engineers (SPIE) Conference Series, Vol. 4841, edited by M. Iye and A. F. M. Moorwood (2003) pp. 1670–1681.
- P. Rosati, I. Balestra, C. Grillo, A. Mercurio, M. Nonino, A. Biviano, M. Girardi, E. Vanzella, and Clash-VLT Team, *The Messenger* **158**, 48 (2014).
- I. Balestra, A. Mercurio, B. Sartoris, M. Girardi, C. Grillo, M. Nonino, P. Rosati, A. Biviano, S. Ettori, W. Forman, C. Jones, A. Koekemoer, E. Medezinski, J. Merten, G. A. Ogrean, P. Tozzi, K. Umetsu, E. Vanzella, R. J. van Weeren, A. Zitrin, M. Annunziatella, G. B. Caminha, T. Broadhurst, D. Coe, M. Donahue, A. Fritz, B. Frye, D. Kelson, M. Lombardi, C. Maier, M. Meneghetti, A. Monna, M. Postman, M. Scodéggi, S. Seitz, and B. Ziegler, *ApJS* **224**, 33 (2016).
- F. Henault, R. Bacon, C. Bonneville, D. Boudon, R. L. Davies, P. Ferruit, G. F. Gilmore, O. Le Fèvre, J.-P. Lemonnier, S. Lilly, S. L. Morris, E. Prieto, M. Steinmetz, and P. T. de Zeeuw, in *Instrument Design and Performance for Optical/Infrared Ground-based Telescopes*, Proc. SPIE, Vol. 4841, edited by M. Iye and A. F. M. Moorwood (2003) pp. 1096–1107.
- R. Bacon, M. Accardo, L. Adjali, H. Anwand, S.-M. Bauer, J. Blaizot, D. Boudon, J. Brinchmann, L. Brotons, P. Caillier, L. Capoani, M. Carollo, M. Comin, T. Contini, C. Cumani, E. Daguis, S. Deiries, B. Delabre, S. Dreizler, J.-P. Dubois, M. Dupieux, C. Dupuy, E. Emsellem, A. Fleischmann, M. François, G. Gallou, T. Gharsa, N. Girard, A. Glindemann, B. Guideroni, T. Hahn, G. Hansali, D. Hofmann, A. Jarno, A. Kelz, M. Kiekebusch, J. Knudstrup, C. Koehler, W. Kollatschny, J. Kosmalski, F. Laurent, M. Le Floch, S. Lilly, J.-L. Lizon à L'Allemand, M. Loupias, A. Manescau, C. Monstein, H. Nicklas, J. Niemeyer, J.-C. Olaya, R. Palsa, L. Parés, L. Pasquini, A. Pécontal-Rousset, R. Pello, C. Petit, L. Piqueras, E. Popow, R. Reiss, A. Remillieux, E. Renault, P. Rhode, J. Richard, J. Roth, G. Rupprecht, J. Schaye, E. Slezak, G. Soucail, M. Steinmetz, O. Streicher, R. Stuik, H. Valentini, J. Vernet, P. Weilbacher, L. Wisotzki, N. Yerle, and G. Zins, *The Messenger* **147**, 4 (2012).
- K. B. Schmidt, T. Treu, G. B. Brammer, M. Bradač, X. Wang, M. Dijkstra, A. Dressler, A. Fontana, R. Gavazzi, A. L. Henry, A. Hoag, T. A. Jones, P. L. Kelly, M. A. Malkan, C. Mason, L. Pentericci, B. Poggianti, M. Stiavelli, M. Trenti, A. von der Linden, and B. Vulcani, *ApJ* **782**, L36 (2014).
- T. Treu, K. B. Schmidt, G. B. Brammer, B. Vulcani, X. Wang, M. Bradač, M. Dijkstra, A. Dressler, A. Fontana, R. Gavazzi, A. L. Henry, A. Hoag, K.-H. Huang, T. A. Jones, P. L. Kelly, M. A. Malkan, C. Mason, L. Pentericci, B. Poggianti, M. Stiavelli, M. Trenti, and A. von der Linden, *ApJ* **812**, 114 (2015).
- E. Jullo, J.-P. Kneib, M. Limousin, Á. Elíasdóttir, P. J. Marshall, and T. Verdugo, *New Journal of Physics* **9**, 447 (2007).
- Á. Elíasdóttir, M. Limousin, J. Richard, J. Hjorth, J.-P. Kneib, P. Natarajan, K. Pedersen, E. Jullo, and D. Paraficz, *ArXiv e-prints* (2007).
- M. Limousin, J. Richard, E. Jullo, J.-P. Kneib, B. Fort, G. Soucail, Á. Elíasdóttir, P. Natarajan, R. S. Ellis, I. Smail, O. Czoske, G. P. Smith, P. Hudelot, S. Bardeau, H. Ebeling, E. Egami, and K. K. Knudsen, *ApJ* **668**, 643 (2007).
- R. Kawamata, M. Oguri, M. Ishigaki, K. Shimasaku, and M. Ouchi, *ApJ* **819**, 114 (2016).
- M. Oguri, *PASJ* **62**, 1017 (2010).
- S. H. Suyu and A. Halkola, *A&A* **524**, A94 (2010).
- S. H. Suyu, S. W. Hensel, J. P. McKean, C. D. Fassnacht, T. Treu, A. Halkola, M. Norbury, N. Jackson, P. Schneider, D. Thompson, M. W. Auger, L. V. E. Koopmans, and K. Matthews, *ApJ* **750**, 10 (2012).
- J. Liesenborgs, S. De Rijcke, and H. Dejonghe, *MNRAS* **367**, 1209 (2006).
- J. Liesenborgs, S. de Rijcke, H. Dejonghe, and P. Bekaert, *MNRAS* **380**, 1729 (2007).
- I. Mohammed, J. Liesenborgs, P. Saha, and L. L. R. Williams, *MNRAS* **439**, 2651 (2014).
- H. C. Plummer, *MNRAS* **71**, 460 (1911).
- M. Bradač, P. Schneider, M. Lombardi, and T. Erben, *A&A* **437**, 39 (2005).
- M. Bradač, T. Treu, D. Applegate, A. H. Gonzalez, D. Clowe, W. Forman, C. Jones, P. Marshall, P. Schneider, and D. Zaritsky, *ApJ* **706**, 1201 (2009).
- I. Sendra, J. M. Diego, T. Broadhurst, and R. Lazkoz, *MNRAS* **437**, 2642 (2014).
- A. Zitrin, T. Broadhurst, K. Umetsu, D. Coe, N. Benítez, B. Ascaso, L. Bradley, H. Ford, J. Jee, E. Medezinski, Y. Rephaeli, and W. Zheng, *MNRAS* **396**, 1985 (2009).
- A. Zitrin, A. Fabris, J. Merten, P. Melchior, M. Meneghetti, A. Koekemoer, D. Coe, M. Maturi, M. Bartelmann, M. Postman, K. Umetsu, G. Seidel, I. Sendra, T. Broadhurst, I. Balestra, A. Biviano, C. Grillo, A. Mercurio, M. Nonino, P. Rosati, L. Bradley, M. Carrasco, M. Donahue, H. Ford, B. L. Frye, and J. Moustakas, *ApJ* **801**, 44 (2015).
- M. Postman, D. Coe, N. Benítez, L. Bradley, T. Broadhurst, M. Donahue, H. Ford, O. Graur, G. Graves, S. Jouvel, A. Koekemoer, D. Lemze, E. Medezinski, A. Molino, L. Moustakas, S. Ogaz, A. Riess, S. Rodney, P. Rosati, K. Umetsu, W. Zheng, A. Zitrin, M. Bartelmann, R. Bouwens, N. Czakon, S. Golwala, O. Host, L. Infante, S. Jha, Y. Jimenez-Teja, D. Kelson, O. Lahav, R. Lazkoz, D. Maoz, C. McCully, P. Melchior, M. Meneghetti, J. Merten, J. Moustakas, M. Nonino, B. Patel, E. Regös, J. Sayers, S. Seitz, and A. Van der Wel, *ApJS* **199**, 25 (2012).
- A. W. Mann and H. Ebeling, *MNRAS* **420**, 2120 (2012).
- L. Christensen, J. Richard, J. Hjorth, B. Milvang-Jensen, P. Laursen, M. Limousin, M. Dessauges-Zavadsky, C. Grillo, and H. Ebeling, *MNRAS* **427**, 1953 (2012).
- J. L. Sérsic, *Boletín de la Asociación Argentina de Astronomía La Plata Argentina* **6**, 41 (1963).
- H. Akaike, *Automatic Control, IEEE Transactions on* **19**, 716 (1974).
- S. Hemmati, S. H. Miller, B. Mobasher, H. Nayyeri, H. C. Ferguson, Y. Guo, A. M. Koekemoer, D. C. Koo, and C. Papovich, *ApJ* **797**, 108 (2014).
- O. Yaron, D. Prialnik, M. M. Shara, and A. Kovetz, *ApJ* **623**, 398 (2005).
- D. Prialnik and A. Kovetz, *ApJ* **445**, 789 (1995).
- M. Kato, H. Saio, and I. Hachisu, *ApJ* **808**, 52 (2015).
- G. Chabrier, *PASP* **115**, 763 (2003).
- J. Wambsganss, in *Gravitational Lensing: Recent Progress and Future Go*, Astronomical Society of the Pacific Conference Series, Vol. 237, edited by T. G. Brainerd and C. S. Kochanek (2001) p. 185.
- C. S. Kochanek, *ApJ* **605**, 58 (2004).
- B. Paczynski, *ApJ* **304**, 1 (1986).
- C. Alcock, C. W. Akerlof, R. A. Allsman, T. S. Axelrod, D. P. Bennett, S. Chan, K. H. Cook, K. C. Freeman, K. Griest, S. L. Marshall, H.-S. Park, S. Perlmutter, B. A. Peterson, M. R. Pratt, P. J. Quinn, A. W. Rodgers, C. W. Stubbs, and W. Sutherland, *Nature* **365**, 621 (1993).
- E. Aubourg, P. Bareyre, S. Bréhin, M. Gros, M. Lachièze-Rey, B. Laurent, E. Lesquoy, C. Magneville, A. Milsztajn, L. Moscoso, F. Queinnec, J. Rich, M. Spiro, L. Vigroux, S. Zylberajch, R. Ansari, F. Cavalier, M. Moniez, J.-P. Beaulieu, R. Ferlet, P. Grison, A. Vidal-Madjar, J. Guibert, O. Moreau, F. Tajahmady, E. Maurice, L. Prévôt, and C. Gry, *Nature* **365**, 623 (1993).
- A. Udalski, M. Szymanski, J. Kaluzny, M. Kubiak, W. Krzeminski, M. Mateo, G. W. Preston, and B. Paczynski, *ACTAA* **43**, 289 (1993).

K. Chang and S. Refsdal, Nature **282**, 561 (1979).
K. Chang and S. Refsdal, A&A **132**, 168 (1984).

D. W. Hogg, I. K. Baldry, M. R. Blanton, and D. J. Eisenstein,
ArXiv Astrophysics e-prints (2002)